

ISSN: 1813-1786
Volume No. 14
Indexed in:
ULRICH'S P. D.
PASTIC

TECHNICAL JOURNAL

2009



**University of Engineering and Technology
Taxila**

ISSN: 1813-1786

Volume No. 14

Indexed in:

ULRICH'S P. D.

PASTIC

TECHNICAL JOURNAL

2009



**University of Engineering and Technology
Taxila**

EDITORIAL BOARD

Prof. Dr. Muhammad Akram Javaid Vice Chancellor, UET Taxila	Patron
Prof. Dr. Muhammad Saleem Mian Chairman EED, UET Lahore	Member
Prof. Dr. Javed Chatha Dean Faculty of Mechanical Engineering GIKI Topi, Sawabi	Member
Prof. Dr. Muhammad Amin Dean, T & IE, UET, Taxila	Member
Prof. Dr. M. A. Kamal Chairman, CED, UET, Taxila	Member
Prof. Dr. Shahab Khushnood Chairman, MED, UET, Taxila	Member
Prof. Dr. Attaullah Solangi Chairman, Software, UET, Taxila, Foreign Faculty from USA	Member
Prof. Dr. Anwar Baig Principal, Institute of Environmental Sciences (IESE), NUST, Rawalpindi	Member
Dr. Mehmood Ashraf Khan Principal, NPGIT, Islamabad	Member
Prof. Dr. Farooq Aslam UET, Lahore	Member
Dr. Shoaib Ahmed Khan CASE, Islamabad	Member
Prof. Dr. M. M. I. Hammouda MED, UET Taxila, Foreign Faculty from Egypt	Member
Prof. Dr. Abdul Sattar Shakir CED, UET, Lahore	Member
Prof. Dr. Ali Rohiem El-Ghalban MED, UET Taxila, Foreign Faculty from Egypt	Member
Prof. Ahmad Khalil Khan Director, ASR & TD, UET, Taxila (Chief Editor)	Member
Prof. Dr. Abdur Razzaq Ghumman Faculty of C&EE (Editor/Secretary)	Member

CONTENTS

	Page No.
1. Effect of Shot Peening on the Fatigue Life of 2024 Aluminum Alloy Arshad Mehmood and M. M. I. Hammouda	01
2. Development and Application of a 2-D Approximation Technique for solving Stress Analyses Problem of a L.P. Turbine using Finite Element Method H. A. Khawaja and A. M. Khan	10
3. A Parametric Study of Deformations and Stresses in Pin-loaded Tubes under Axial Tension Ishtiaq Ahmad	16
4. Development of Novel Method for the Selection of Material for Axial Flow Compressor Blade M. Javed Hyder and M. Omair Khan	22
5. Effects of Cutting Parameters in Erosion Failure of Ductile Materials in Abrasive Water Jet Machining Asif Iqbal, Naeem Ullah Dar and Mubasher Chohan	27
6. Ultrasonically Assisted Turning: Finite Element Model N. Ahmed , M. Abid , A.V. Mitrofanov and V.V.Silberschmidt	33
7. An Analytical Finite Element Model for Tool-Chip Contact Area for Orthogonal Cutting Muhammad Shoaib	43
8. Analysis of Thickness Effect on Piezoelectric Beam Riffat Asim Pasha, Zahid Suleman and M. Z. Khan	50

Effect of Shot Peening on the Fatigue Life of 2024 Aluminum Alloy

Arshad Mehmood¹ and M. M. I. Hammouda²

Abstract

Experimental study of the effect of shot peening parameters such as shot size, nozzle pressure, nozzle distance, impingement angle and exposure time on high strength Aluminum alloy ASTM 2024 mostly used in air craft industries for cyclic loading applications has been presented. In the first part of research work, following the standard procedure, effect of peening parameters on the Almen strip and finally on the fatigue test specimens was studied. Surface texture changes occurred due to peening was examined using powerful optical microscope. Peening process also led to the formation of compressive residual stresses in the surface layer and was determined using "hole drilling" method. Based on the results, a set of optimum peening parameters was evolved. Machined (unpeened) specimens and peened specimen were tested using four point rotating bending fatigue testing machine to generate the SN-curves. The results indicated a considerable improvement in the fatigue life of peened specimens when compared with the fatigue life of unpeened specimens.

Keywords: Shot Peening, Fatigue Life, Parameters, Aluminum Alloy

Introduction

Shot peening is a well-established cold working process, widely used in automotive and aircraft industries. [1] The technique involves the impingement of a stream of spherical shots, directed at the metal surface at high velocity under controlled conditions [2, 14]. The process has useful applications in increasing fatigue strength, relieving tensile stresses that contribute to stresscorrosion cracking, forming and straightening of metal parts, and testing the adhesion of silver plates on steel [2,12].

Shot peening generates plastic deformation in the exposed surface layer and, thus, induces compressive residual stresses in that layer [14]. Thus, an improvement in the fatigue strength of shot peened components is commonly reported in the literature [1, 7, 9, 10, 16, 20]. Such an effect depends on the variables of the process, i.e. shot size, nozzle pressure, impingement angle, shot flow rate and nozzle distance from the specimen surface. Those variables are integrated in the form of Almen intensity [3, 7,10,16,]. Aerospace industry has a particular interest in aluminum alloys. Examples of relevant peened parts include fuselage skin, wing ribs, bulkheads, landing gear beam and wing lower skin of air crafts. Helicopter rotor blades and some parts of their drive elements, high-pressure turbine and compressor discs are other examples. Some of those parts are made of Aluminum alloy 2024.

Fatigue life against shot peening of specimens made of aluminum alloys was experimentally investigated [12, 13, 16-17]. There are reports indicating variations in the fatigue life for peened components. References [1, 7, 9, 10, 16, 20] have shown that shot peening has beneficial effects on the different grades of aluminum alloys.

On the other hand studies [4] have shown that steel shot peening (steel shot diameter between 0.35 and 0.7 mm to an Almen intensity of 0.010A, per SAE J442 standard) did not result in an increase in the fatigue endurance of aluminum alloy.

In some cases the fatigue limit of the shot peened specimens fell below that of the un-peened specimens for example studies [6] have shown that steel shot peening with shot S 110 and S280 as per SAE J442 standard has decreased the fatigue life of aluminum alloys. [6]

For the best results, it is essential to optimize the various peening parameters. Analysis of the shot peening variables in terms of the total energy of the shot stream shows that for a given material being peened, a maximum value of surface stress is reached and stays constant over a wide range of energies. An optimum value of shot stream energy exists to obtain maximum fatigue life. This is related to shot size and flow rate through the physical effects of the shot impacting the work surface [7].

^{1&2} Department of Mechanical Engineering, University of Engineering & Technology Taxila.

The results of different worldwide research works presented above indicates the importance of process quality control and peening parameters in peening Aluminum alloys in terms of achieving the optimum improvement in fatigue life. This is not a simple problem and a number of parameters have to be carefully controlled to maximize fatigue life. These include peening media (Shot size, shot material, shot quality), pressure /velocity, Exposure time, peening distance etc. [1].

These references (4-7, 11-12) reveal that shot peening process depends upon peening condition or peening parameters. But it remains unclear how these parameters affect the peening quality and what are the optimum peening conditions for Aluminum alloys. Also, these inconsistent reports do not provide the high level of confidence required for the industrial adaptation of the process in the basic design considerations as long as fatigue strength is concerned. Detailed literature review and above presented results highlights further research areas and may be considered sufficient justification to the selected research work. The research undertaken will provide a good understanding of peening process, optimum peening parameters affecting the fatigue life of aluminum alloys and residual stress measurement.

EXPERIMENTAL WORK

Material and Specimen

The material in the present work was 2024 Aluminum alloy ASTM-B211. Table 1 lists the mechanical properties of the tested material. The corresponding chemical composition in weight % was as follows: 0.1 Cr, 2.0 Cu, 0.5 Fe, 1.5 Mg, 0.6 Mn, 0.05 Si, 0.15 Ti, 0.25 Zn and remaining Al. Fig.1 shows the geometry of the present fatigue test specimen as per ASTM standard E606 [15]. Forty-five of such specimens were tested to obtain their S/Nf curve in both condition of as machined and after purposely-designed shot peening.

Table 1: Mechanical properties of Aluminum 2024 ASTM-B211

0.2 % Proof stress MPa	Ultimate tensile stress MPa	Elongation %	Possion's ratio	Elasticity modulus GPa	Brinell Hardness
324	393	20	0.33	73.1	120

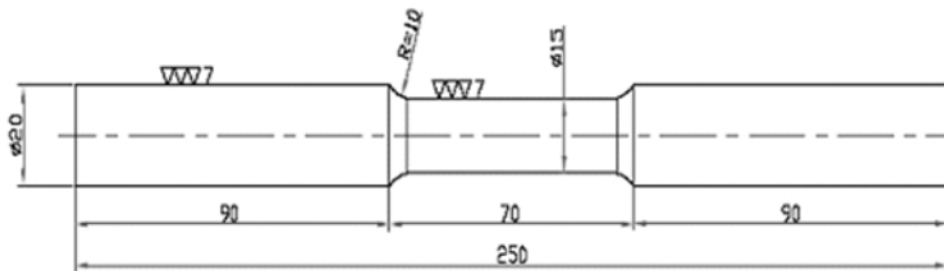


Figure 1: Geometry of the present test specimen

Evaluation of Almen Intensity

Shots of three sizes were applied for this process. Their material / hardness are listed below in table 2. Experimental work started from peening machine. An air blast machine of 136 MPa pressure rating was selected for the test work. The air blast nozzle internal diameter (6mm) was checked using a standard go-no go gauge before testing. Shot flow rates were calibrated using real time catch tests. The nozzle to test strip / specimen center location was adjusted and was checked before and after testing, the shot impact angle on the test strips was calibrated and checked before and after testing protractor/level. Peening strips of size 3"x 0.75"x 0.031" thick (type A) as per SAE J442 arranged. "A" scale / type Almen strip is recommended for low intensities which are normally used for soft materials like aluminum [3]. Three standard sizes for strips of material SAE 1070 spring steel are used and "A" scale type is shown in the fig.2

[14] Each strip was individually inspected for flatness using an Almen Gage #2. All strips with a tolerance of less than or equal to 0.0001 inch were selected for use. All strip mountings and removals were done using a systematic method. These strips were screwed on a solid block and then on the perforated plate of the peening machine as shown in the fig. 3[14].

Table 2: Peening Media Properties [14]

S.No	SAE No.	Ø (inches)	Material	Hardness (HRC)
01	S110	0.0197	Cast steel	45
03	S170	0.0280	Cast steel	45
04	S230	0.0394	Cast steel	45

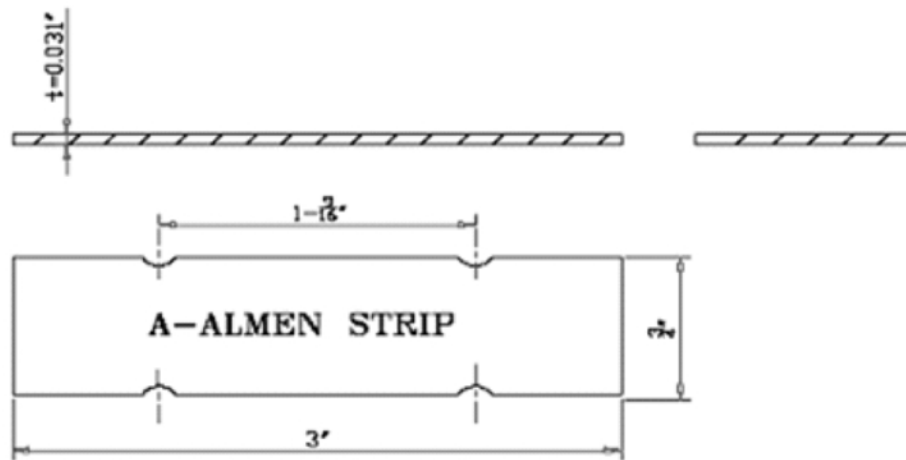


Figure 2: "A" Type Almen Strip

Several experiments were performed on Almen strips. Each individual peening process parameter (like shot size, nozzle pressure, impingement angle, exposure time and nozzle distance from the specimen) was varied to determine the relationship with almen height. During each experiment other parameters were kept constant. Finally we were left with individual parameter Almen intensity and its affect on the fatigue life of actual specimen were experimentally determined.

Peening of fatigue test specimen

The same procedure was adopted for the peening of fatigue test specimen as described for Almen strip. Following parameters were selected for the peening of fatigue test specimen.

Process variables	Nominal setting
Nozzle pressure	60-80 psi
Nozzle internal diameter	6mm
Shot sizes:	S-110, S-170, and S-230
Nozzle to specimen distance	7 inches
Shot impact angle:	65°
Specimen motion	25 rpm

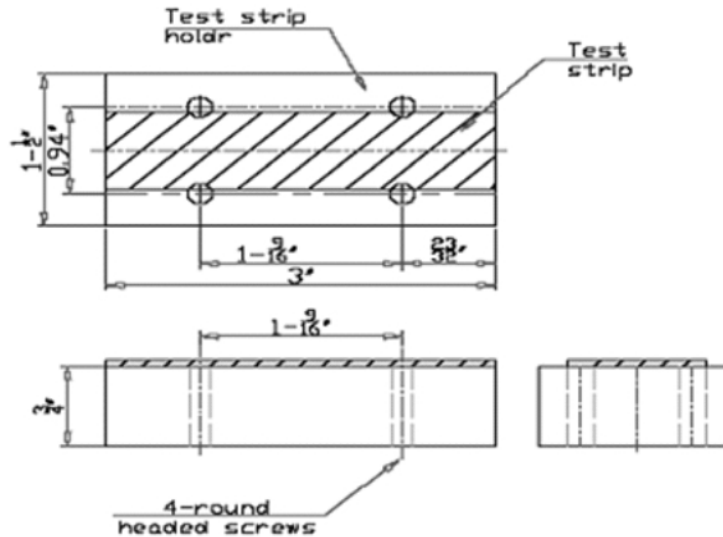


Figure 3: Almen Strip Holder

Fatigue Testing

The fatigue test programme was carried out utilizing a four points rotating bending machine of 20kg-m maximum bending moment and 2860 rpm speed. The preliminary investigations concentrated on establishing base line information regarding the fatigue life of the material. In the main part of the programme as machined and shot peened specimens were utilized and SN curves were determined with the view of examining the effects on peening parameters on the fatigue life in the presence of alternating stresses. All tests were performed with the load ratio of $R = -1$

Results and discussion

Results of the first part of experimental work are related to the evaluation of Almen intensity, which depends on different variables like air pressure, impingement angle, nozzle distance and shot flow rate. Relationship between each individual variable and Almen intensity was obtained by keeping the other three parameters constant and are mentioned on each graph.

In fig. 4 nozzle pressure versus Almen height graph is shown. Air pressure exhibited nearly linear behavior regarding intensity until the maximum value is obtained. The combined effect of peening parameters appears in the form of Almen height which is the indication of absorbed energy in the almen strips. It is obvious that higher pressure causes higher values of shot velocities and hence more energy will be transmitted, consequently higher values of almen intensities will appear. Effect of nozzle pressure is related to shot sizes. Larger shots give higher almen intensities than that of smaller shots. Up to certain value of pressure almen height increases and then once again curve bows down. It can be concluded that optimum value of pressure exists somewhere and can be achieved.

In fig.5 relationship between nozzle angle and Almen height is shown. Nozzle angle had the greatest effect on intensity. Changes in nozzle / impingement angles have a pronounced effect at low angles and very little effect at angles greater than 65° . At low angles, this effect is almost parabolic, implying the lower the angle, the greater the effect.

The high velocity shots stream imparts energy in the peening strip. Between 0° and 90° shot velocity is resolved into two components i.e. Normal and horizontal. According to Hertzian pressure [21] the normal component of shot velocity produces impact load which causes a maximum shear stress below the surface and it has key role as far as Almen intensity is concerned. As impingement angle increases normal component increases and its effect reaches certain maximum value and after that the curve is almost horizontal. It can be concluded that the value of normal component of shot velocity has maximum effect at 65° and after that up to 90° this effect is almost negligible.

Fig.6 shows that Almen height increases by increasing the nozzle distance until the maximum value is achieved and after that value Almen height once again decreases. But it can be concluded that overall effect of nozzle distance is limited and is inversely proportional. At smaller nozzle distances and larger distances shot stream can not produce the desired effect. Fig.7 shows that media flow rate is inversely proportional to the intensity.

Table 3: Residual Stresses Measurement

S.No	Almen Intensity	Residual Stress (Max.) MPa	Depth (mm)	Residual Stress (Min.) MPa	Depth (mm)
01	8A	-219	0.2	40	0.5
02	10A	-230	0.4	45	0.5
03	12A	-242	0.2	49	1.4

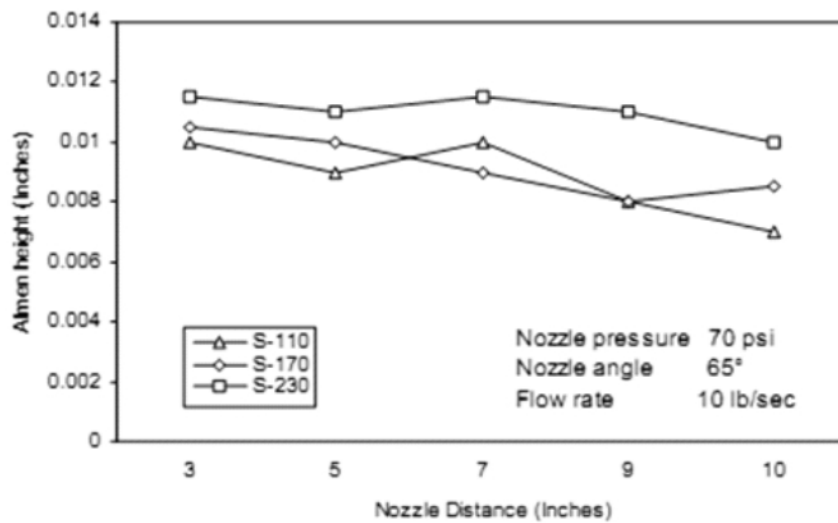


Figure 4 & 5: Nozzle pressure vs. Almen height & Nozzle distance vs. Almen height

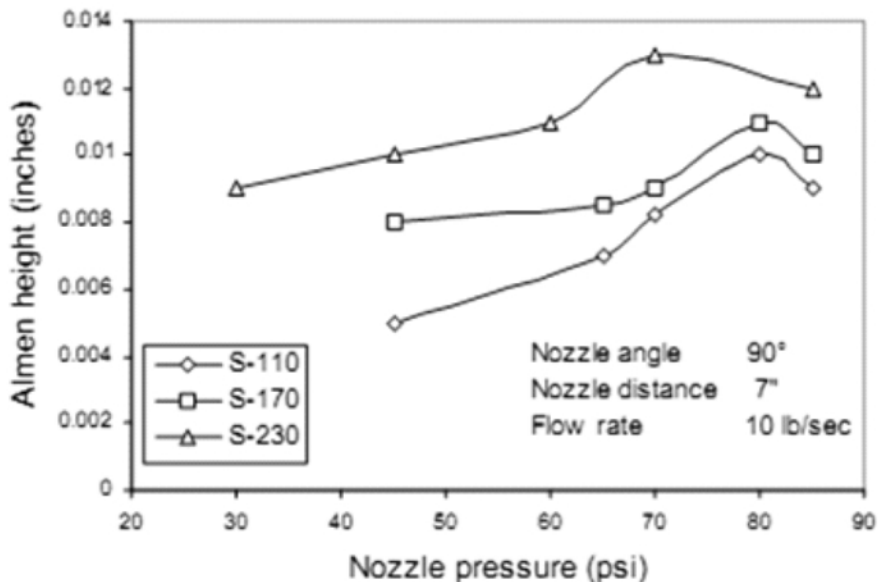


Figure.6 Nozzle angle vs. Almen height

Microstructure changes occurred due to shot peening were also examined using powerful optical microscope. In fig.7 and fig. 8 microphotographs of as machined and peened specimens are shown. It can be visualized that peening has produced indentation / compression in the specimen and has spread material near the impact point against the resistance of neighboring material, thus introducing a complex sub-surface residual stress distribution in which generally, the surface is in elastic compression. Stresses produced due to peening were determined by hole drilling method shown in the table: 3 [14]

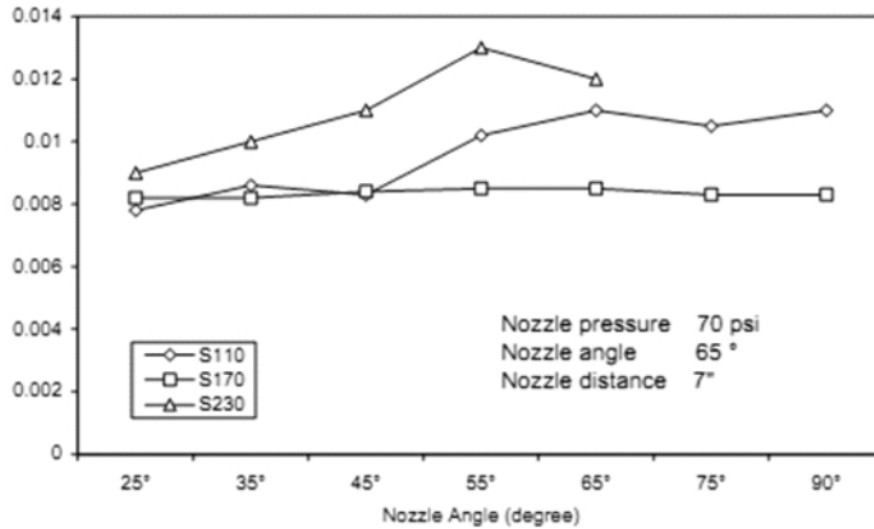


Figure 7: Shot flow rate vs. Almen height

In the second part of experimental work effect of shot peening on the fatigue life of Aluminum 2024 is determined. Peening process produces residual stresses in the surface layers of peened specimens. A comparison between as machined and shot peened specimens is shown in fig.8 and 9. Microphotographs of machined (before shot peening) and after peened were obtained using powerful microscope. Each shot acts like a hammer and produces residual stresses in the surface and subsurface layers. It can be visualized that peening has produced indentation / compression in the specimen and has spread material near the impact point against the resistance of neighboring material, thus introducing a complex sub-surface residual stress distribution in which generally, the surface is in elastic compression. Stresses produced due to peening has been determined using hole drilling technique and shown in table 3. For higher values of Almen intensity value of residual stresses will be higher.

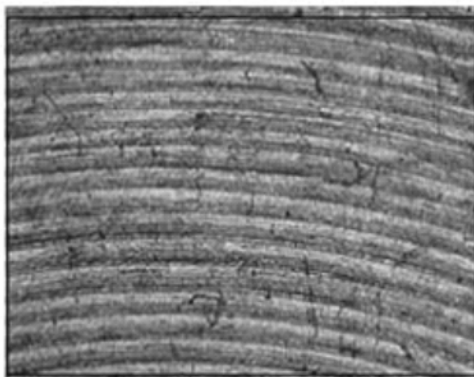


Figure 8: Microphotograph of machine surface with 50x magnification

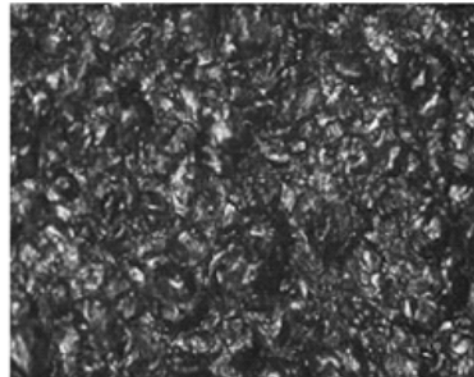


Figure 9 Microphotograph of peened surface with 50x magnification

Considerable improvement in the fatigue life of peened component was observed. In table 4 results of as machined and shot peened specimens are shown. 166 % improvement has occurred due to shot peening at the cyclic stress of 60 % of the UTS. This is because of residual stresses produced by shot peening. These stresses slow down crack propagation rate.

At lower stress values fatigue life improvement will be more as compared to higher stress values. As cracks propagation rate is higher at higher stress values.

Almen intensity is the major parameter on which fatigue life of the specimen depends. Number of cycles versus Almen height graph shows that up to certain value of Almen intensity, number of cycles increases and then curve bows down even by increasing the Almen height. This may be due to the residual stress value that should be optimized otherwise peening may produce adverse effects.

The fatigue life that can be visualized from fig.10. This is because of compressive residual stresses. Larger size media produces more residual stresses than the smaller one which may decrease the fatigue life of specimens. Almen intensity can be optimized from the results of figure: 11. Up to certain value of Almen intensity fatigue life increases and after 12A it once again decreases. Hence 12A can be considered optimized value of Almen intensity.

Table 4: Fatigue life comparison of as machined and 12A-shot peened specimen at an applied stress of 250 MPa (63% , 38% of UTS)

S.No	σ_b / W MPa-Kg	As machined N_f	Average N_f	Peened-12A N_f	Average N_f	Gain	%(Gain)
01	250/ 66	1.145×10^4	1.898x 10^4	4.85×10^5	5.06x 10^4	3.1x 10^4	166%
02		2.40×10^4		4.70×10^5			
03		1.80×10^4		4.23×10^5			
04		2.25×10^4		6.46×10^5			
01	150/40		1.25×10^5		8.3×10^5	6.05×10^5	484%

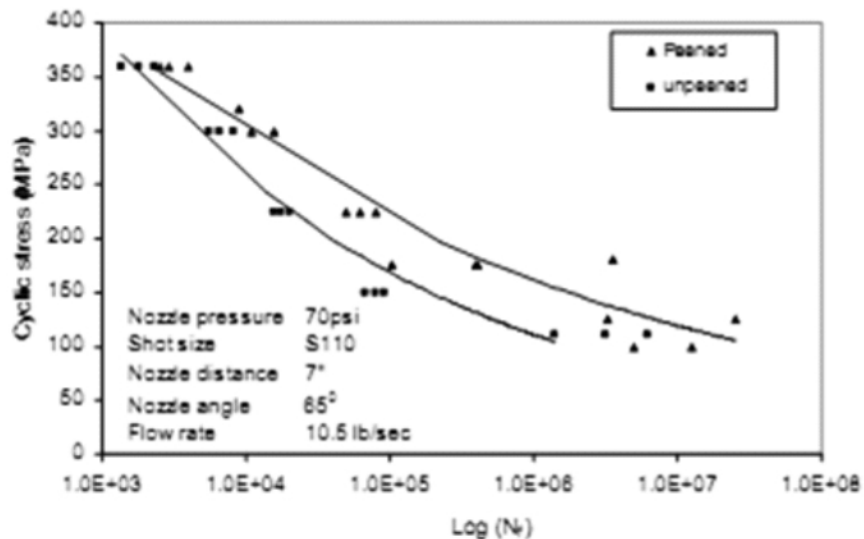


Figure 10: SN curves comparing the fatigue life of unpeened and 12A peened specimens

Conclusions

The effect of shot peening on fatigue life of the 2024 Aluminum alloy was studied under constant amplitude loading condition. The results showed that shot peening can be applied to increase the fatigue life of the aluminium alloy under optimum conditions otherwise we may not get the appropriate results and even it may cause adverse effects. Also the beneficial effect of the process is greater at long fatigue lives than at short fatigue lives.

1. Air pressure exhibits nearly linear behavior regarding intensity until the maximum intensity for a particular media size is achieved. Higher intensities can be obtained at lower pressure for large size shots.
2. Nozzle angle had the greatest effect on intensity. Changes in nozzle/impingement angles have a pronounced effect at low angles and very little effect at angles greater than 55° for small shots and 65° for large diameter shots.
3. Nozzle distance has a limited effect on intensity and media flow rates is inversely proportional to the intensity. Value of Almen intensity increases as media size increases.
4. Larger size shots produce more residual stresses in the surface layers of the specimen as compared to smaller size shots and smaller shots are more effective than the larger shots.
5. Optimum value of the peening intensity exists between 8A to 13A for aluminium alloys.

Acknowledgements

National Institute of Science and Technical Education, Islamabad.

References

- [1] Akber J.A, Kyriacou S., El-Zafrany A.M “ Effect of Shot Peening on the Fatigue Life of Axially Loaded Notched Components” , Conf Proc: ICSP-5, Willey Publisher ,13-17 September,1993, pp.349-358
- [2] H. O. Fuchs and E. R. Hutchinson, Shot Peening, Machine Design, Vol.30, Feb. 6,1958, p. 116-125
- [3] H.O. Fuchs,” Defects and Virtues of the Almen Intensity”, Conf Proc: ICSP-2, Willey Publishers, September 14-17,1984, pp 74-78,
- [4] Sharp, P K; Clayton, J Q; Clark, G “ The Fatigue Resistance of Peened 7050-T7451 Aluminum Alloy, Repair and Re-Treatment of a Component Surface” Fatigue Fract. Eng. Mater. Struct. Vol. 17, No. 3, pp. 243-252. Mar. 1994
- [5] Zhuang, W. Z. and Halford, G. R. “Investigation of residual stress relaxation under cyclic load”, Int. Journal of Fatigue, Volume 23, Supplement 1, 2001,pp. 31-37
- [6] Sharp, P K, Clark, G” The effect of peening on the fatigue life of Aluminum alloys” Advances in Fracture Research. ICF9. Vol. 3. Fatigue of Metallic and Non-Metallic Materials and Structures; Sydney; Australia; 1-5Apr. 1997. pp. 1491-1499, 1997
- [7] J. A. Horwath ” Effect of Shot Peening Variables on Bending Fatigue” Conf Proc: ICSP-1 Willey Publishers ,14-17 September,1981, pp 229-236. 8. Richard C, Wieland “A Statistical Analysis Of The Shot Peening Intensity Measurement” ICSP5, Oxford, U.K.,Willey Publisher,13-17 September,1993, (Advanced Metal Process, Doc. #1993015,1993)
- [9] Barter, S.L “Repair and Life Assessment of Critical Fatigue Damaged Aluminum Alloy Structure Using a Peening Rework Method” Journal USAF ASIP Conference 5-7 December,2000, San Antonio, TX, USA, /Australian Science Magazine, DSTO
- [10] Jian,L. Editor, Hand book of Measurement of Residual Stresses, Society For Experimental Mechanics, Inc., The Fairmont Press, 1996 Inc. Chapter 1(p1-4) & Chapter 5(p71-78).
- [11] Predictive Models For Small Fatigue Cracks Growing Through Residual Stress Fields C. H. Wang And Q. Li

- [12] S. T Kim, D. Tadjiev, " Fatigue Life Prediction under Random Loading Conditions in 7475-T7351 Aluminum Alloy using the RMS Model" Int. Journal of DAMAGE MECHANICS, Vol. 15- January 2006, (pp89-101)
- [13] Roger. S "Effects of Peening on Fatigue Life of Wrought 5454 Aluminum Automotive Road Wheels" Conf Proc: ICSP-2, Willey Publishers ,14-17 May,1984, pp. 58-62
- [14] Puchi-Cabrera. E. S, Villalobos-Gutie´rrez. C. I. Irausqui´n, L´arberaosa, G.
- [15] Mesmacque " Fatigue behavior of a 7075-T6 aluminum alloy coated with an electroless Ni-P deposit"Int.J of Fatigue, Vol.28 2 Dec,2005 , pp-1854-1860
- [16] Rodopoulos C. A, Curtis S. A. de los Rios, E. R. Solis Romero. J, " Optimisation of the fatigue resistance of 2024-T351 Aluminum alloys by controlled shot peening- methodology, results and analysis", Int. J of Fatigue, Vol. 26 2 19 Jan,,2004 , pp-849-856 Benedetti. M., Bortolamedi. T., Fontanari. V., Frenzo.F "Bending fatigue behaviour of differently shot peened Al 6082 T5 alloy" Int. J of Fatigue, Vol.26 2 17 Dec,2004 , pp889-897.
- [17] Sonsino C. M. , Radaj D., Brandt U., Lehrke H.P., " Fatigue assessment of welded joints in AlMg 4.5Mn Aluminum alloy (AA 5083) by local approaches" Wang Q. Y, Kawagoishi.N., Chen. Q. "Fatigue and fracture behaviour of structural Al-alloys up to very long life regimes" Int. J of Fatigue, Vol.28, 19 Sep.2005 , pp-1572-1576
- [18] Turkmen H. S., Loge R. E., Dawson P. R., Mill M. P., "On the mechanical behaviour of AA 7075-T6 during cyclic loading" Int.J of Fatigue, Vol.25, 8 Oct.2003 , pp-267-281
- [19] Ali A., An. X., Rodopoulos C. A., Brown M. W., Hara P. O., Levers A., Gardiner S., "The effect of controlled shot peening on the fatigue behaviour of 2024-T3 Aluminum friction stir welds" Int. J of Fatigue, Vol.30, 16 Oct.2006 , pp-267-281

Development and Application of a 2-D Approximation Technique for solving Stress Analyses Problem of a L.P. Turbine using Finite Element Method

H. A. Khawaja¹ and A. M. Khan²

Abstract

With the advent of computational techniques and methods like finite element method, complex engineering problems are no longer difficult to solve. However, applying these techniques is not a simple task and require lots of acumen, understanding and experience in obtaining solution which is as close to exact solution as possible with minimum computer resources. In this work using finite element) method, stress analyses of low pressure turbine of a small turbofan engine is carried out by employing two different techniques. Initially, complete solid model of the turbine is prepared which is then finite element meshed with eight-node brick element. Stresses are calculated using this model. Subsequently, the same turbine is modeled with four-node shell element for calculation of stresses. Material properties, applied loads (inertial, aerodynamic, and thermal), and constraints were same for both the cases. Authors have developed a "2-D approximation technique" to approximate a 3-D problem into a 2-D problem to study the saving in valuable computational time and resources. In this statistics technique, the variable thickness blade is divided into many small areas of constant thickness. It is ensured that the value of the thickness for each sub-area is correct representative thickness of that sub area and it is within three sigma limits. The results revealed that technique developed is accurate, less time consuming and computational effort saving; the stresses obtained by 2-D technique are within five percent of 3-D results. ANSYS ® 9.0 was used of this work.

Keywords: 2-D Approximation Technique, Finite Element Method, Low Pressure Turbine

Introduction

Stress analysis in any engineering field is invariably complex, and obtaining exact solution is almost impossible if geometry is complicated. In such a situation, engineers usually resort to numerical approximate methods to solve the problems. With the advent of computers, one of the most powerful techniques that have been developed in the realm of engineering analysis is the FE method, and the method, being general, can be used for the analysis of structures / solids of complex shapes and complicated boundary conditions. However employing this method correctly is in itself a challenging task.

Today computational power is much larger, more reliable, and relatively cheap and as most technology related setups have access to computers, the popularity of using numerical methods is an ever increasing phenomenon. Especially FE method is being used at large extent for structural analysis. Description of the development of the FE method and its application is thoroughly discussed [1, 2]. V.Ramamurti, D. A. Subramani and K. Sridhara [3] have analyzed vibration using FE method. Also A.M. Khan, M. N. Ahmed and S. Mushtaq [4] have used FE method for stress analysis. Otherthan discussed, ANSYS® Inc. has verified FE method by providing s number of verification manuals for static, modal, harmonic, etc analysis [5], thus proving our point that FEM provides reliable solution to engineering problems. Additionally, there is a lot of literature available on finite element analyses of complex structures.

In this work, we have made an effort to solve complex 3-dimensional stress analysis problem of a low pressure turbine of a small turbofan engine first by using '2-dimensional approximation technique' in order to take advantage of reduced computational time and ease of finite element modeling and meshing. The same problem was also solved by modeling the blade with 3-D, 8 noded brick type of finite element. Comparison of results obtained from both methods is made and discussed. For this work commercially available FE software ANSYS® was used as a tool for the analysis.

Dimensional Approximation Technique

Any structural element whose one of the dimension (thickness) is one order of magnitude smaller than rest of the two, can be termed as "thin walled structure". Finite Element stress analysis of such structures is

^{1&2} Department of Aerospace Engineering, College of Aeronautical Engineering, NUST

generally conducted using 2-D shell type of elements. A difficulty arises once the thickness of the structures is not constant, but it is variable e.g. turbine or compressor blades. In that situation, the thickness has to be approximated while carrying out the finite element analyses, using some thickness approximation technique so that the accuracy of results is not compromised.

Dimensional approximation technique that we have used requires a bit of modeling work. However its finite element model is relatively easy to built and easy to mesh compared to 3-dimensional model. We developed the 3-Dimensional CAD model of turbine blade after lots of discussion with aerodynamics and propulsion designers. Its 3-dimensional shape is shown Fig. 1. There are 59 blades in the turbine joined with solid hub. Blades have thicker aerofoil at hub in comparison to tip. Also geometric and aerodynamic twist is there to have best possible performance from turbine.

In order to cater for the blade thickness in 2-D finite element model, a simple 2-D approximation technique was applied in which the entire blade was distributed into many sub areas whose thickness was assumed constant. The value of that thickness was in fact the average thickness of that area. The blade was distributed into many areas having constant thickness, which was the average value of the actual variable thicknesses of blade in chord and span directions as illustrated in Fig. 2, where A, B, C, D, E, and F are thicknesses associated with one subarea as shown. The methodology to reach to the final number of subarea in which the blade was eventually distributed into, is explained in subsequent paragraphs. Division of areas were made in such a way that maximum and minimum value of thicknesses in a subarea remains within 3-sigma limits. Initially the blade was divided into three subareas, but the value of average thickness did not fall within the 3-sigma limits.

Subsequently, the blade was divided into more and more subareas till the thickness of each subarea was within 3-sigma limit. After the determination of thicknesses, the mean chamber line of tip and root aerofoil were modeled and joined, keeping areas of different thicknesses as separate entity.

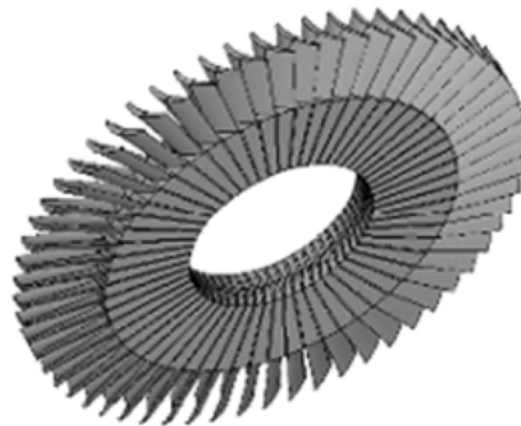


Figure 1: CAD Model of Turbine

Table 1: Thicknesses associated with 2-D approximated areas

<i>Area No.</i>	<i>Maximum Thickness (mm)</i>	<i>Minimum Thickness (mm)</i>	<i>Average Thickness (mm)</i>	<i>Standard Deviation(mm)</i>
1	0.845	0.811	0.828	0.012
2	1.804	1.771	1.787	0.011
3	2.130	1.928	2.029	0.071
4	2.666	2.212	2.439	0.160
5	2.982	2.293	2.638	0.243
6	2.589	1.975	2.282	0.217
7	2.075	1.674	1.875	0.142
8	0.939	0.782	0.860	0.055

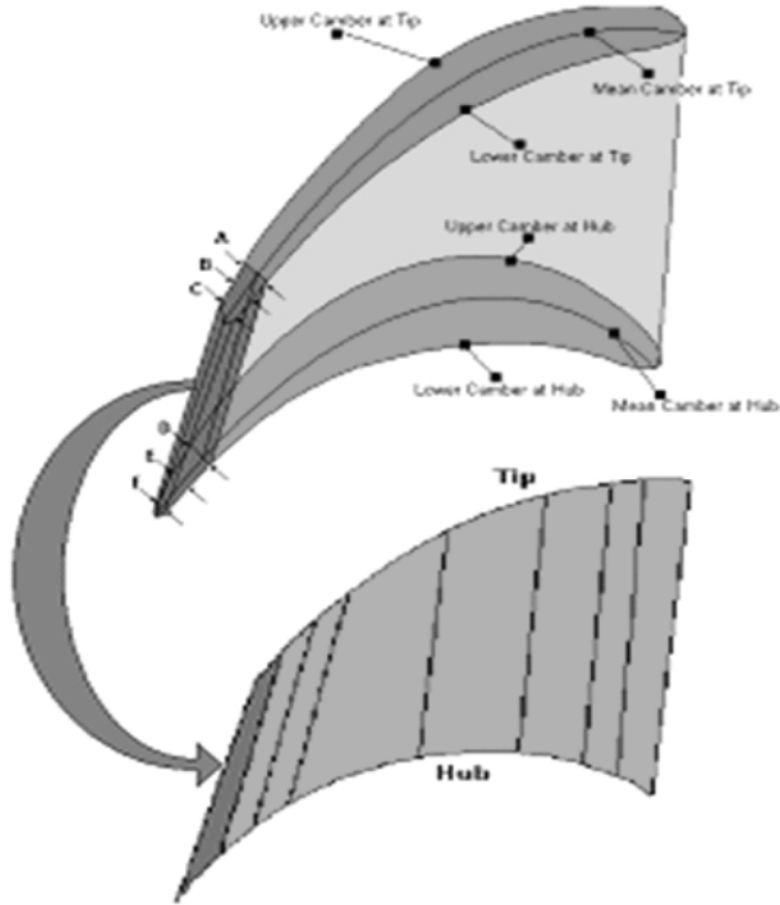
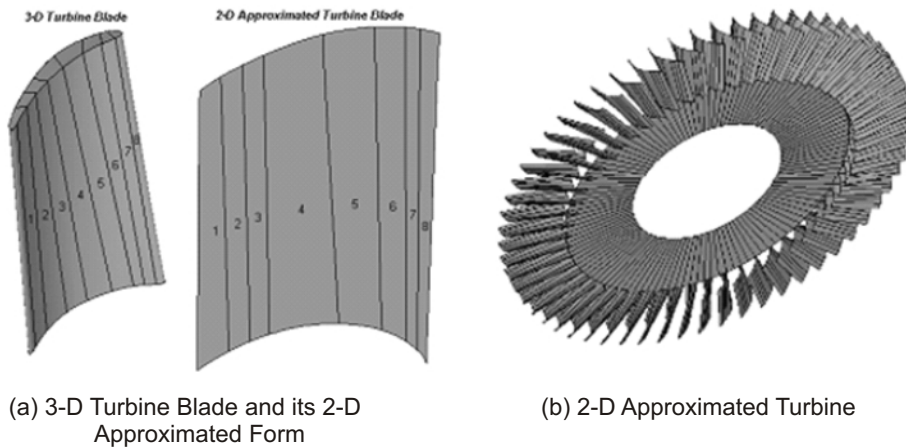


Figure 2: Illustration of thicknesses taken from 3-D turbine blade for making 2-D areas

Maximum value of thickness, minimum value of thickness, average value of thickness and standard deviation from average value for each area within the blade is shown Table 1. Areas built for turbine blade using 2-D approximation technique are shown in Fig. 3(a). Turbine disc (Hub) is approximated with an area having constant value of thickness equal to 3mm. Turbine model build using 2-dimensional approximation is shown Fig. 3(b).



(a) 3-D Turbine Blade and its 2-D Approximated Form

(b) 2-D Approximated Turbine

Figure 3: 2-D Approximated blade and complete turbine

Finite Element Modeling and Applied Constraints

The 2-D approximated model of turbine was meshed with 4 Node Shell 63 elements of ANSYS, as shown in Fig. 4(a). Figure 5(a) shows the blade-hub Joint which was modeled by node coupling. Mesh sensitivity analysis was carried out to have a mesh with an optimum number of nodes. Optimized mesh is capable of giving accurate results with minimum utilization of computational resources. 3-D model of blade was created from many small volumes, which were glued and meshed with an 8 Node Brick 45 element type "Fig. 4(b). Mesh sensitivity analysis was also carried out on 3-D FE model of turbine. Optimized mesh was selected for analysis performed.

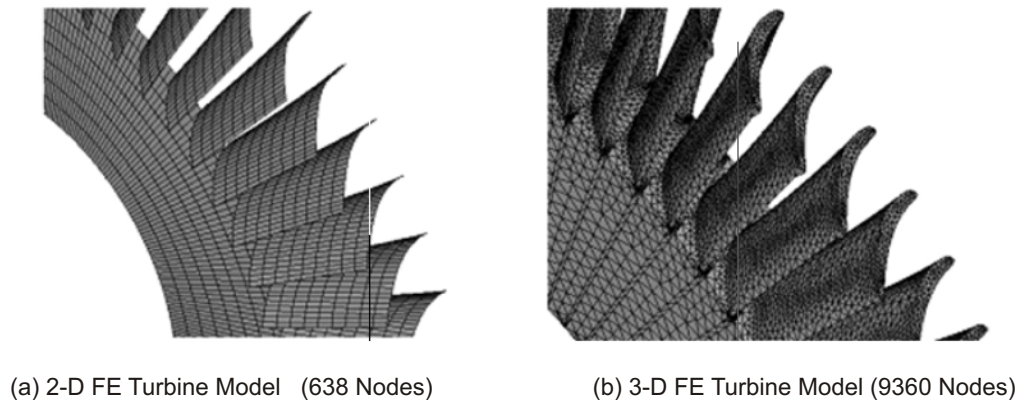


Figure 4: Finite Element Model of Turbine

Before running FE solution, displacement constraints were also defined; for that all nodes at turbine-shaft linkage "Fig. 7" were constrained in all degree of freedoms. Both analyses were carried out using linear-elastic material model. Mechanical properties of Nickel based alloy Inconel 718 were taken for analysis of turbine [6].

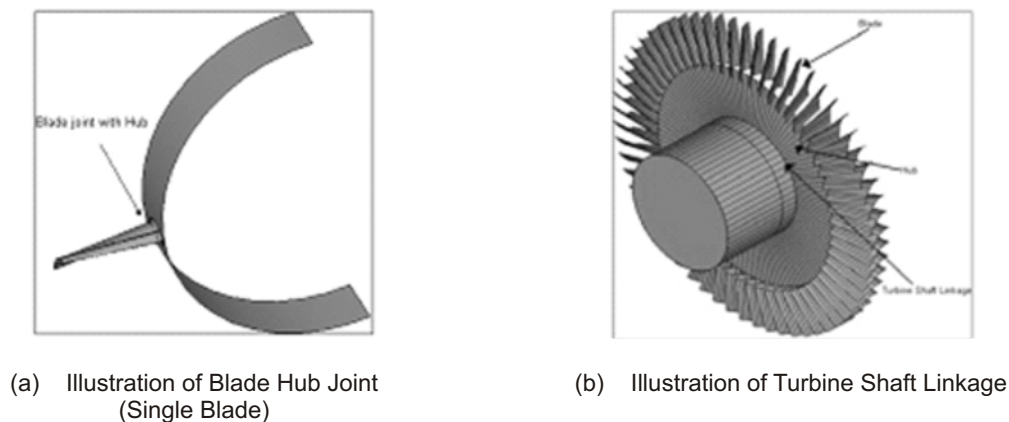


Figure 5 Blade Hub Joint and Turbine Shaft Linkage

Linear Static Analysis and Applied Loads

Turbine blades are subjected to various types of loadings such as aerodynamic, thermal and inertial loads; values can be seen in Table 2. Aerodynamic load, the difference of pressure acting on upper and lower surface of blade, was applied as distributed load on the lower surface of turbine blade. Thermal load was applied on the entire blade and inertial load was applied as body load which is due to the rotation of the turbine.

Linear Static Analysis Results

Number of nodes required by 2-dimensional approximate model is almost 15 times lesser than number of nodes required for analyzing 3-dimensional model, and it was found out that solution time is six times lesser for 2-dimensional approximated model than 3-D model. Von-Mises (Effective) stress contour plots of 2-dimensional approximated and 3-dimensional blade as per static analysis for normal operational load are shown “Fig. 6”. Also displacement contour plots of both the blades under normal operational load are given “Fig. 7”.

Table 2: Loading conditions on turbine as per defined cases

<i>CASE 1</i> (Normal Operation)	Maximum Pressure	0.5745 MPa
	Maximum Temperature	1056.55 K
	Operating RPM (Inertia)	32200 RPM
<i>CASE 2</i> (Over-run Operation)	Maximum Pressure	0.6320 MPa
	Maximum Temperature	1083.33 K
	Operating RPM (Inertia)	38000 RPM
<i>CASE 3</i> (Normal Operation)	Maximum Pressure	0.4309 MPa
	Maximum Temperature	972.22 K
	Operating RPM (Inertia)	32200 RPM
<i>CASE 4</i> (Over-run Operation)	Maximum Pressure	0.5027 MPa
	Maximum Temperature	1027.78 K
	Operating RPM (Inertia)	38000 RPM

Comparison of results is given “Table 3”. The difference between 2-D model and 3-D model for normal operation for maximum stress is 6.30 % where as far as maximum displacements it is 4.00 %.

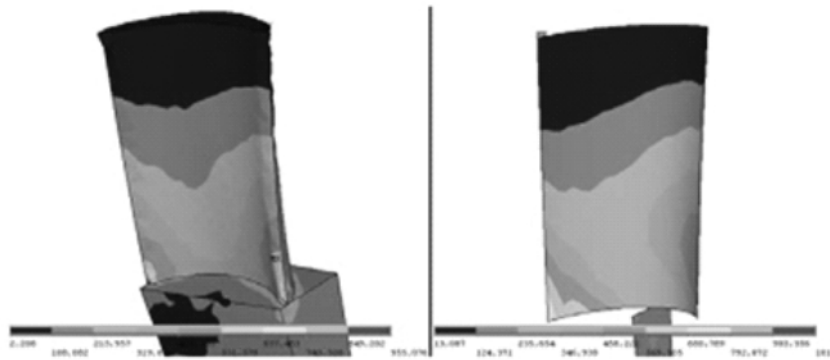


Figure 6: Effective Stress (MPa) Contour Plot of Turbine Blade for Normal Operation

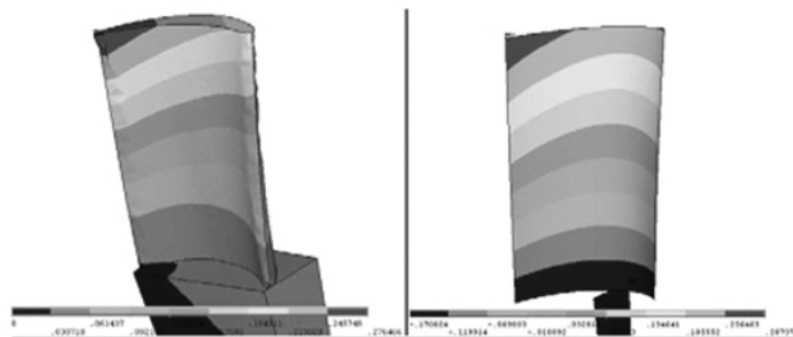


Figure 7: Displacement (mm) Contour Plot of Turbine Blade for Normal Operation

Table 3: Comparison of results obtained by Stress Analysis

<i>Load Cases</i>	<i>Max. Values</i>	<i>3-D blade</i>	<i>2-D blade</i>	<i>% Difference</i>
<i>CASE 1 (Normal Operation)</i>	Stress (MPa)	955	1015	6.30 %
	Displacement (mm)	0.276	0.287	4.00 %
<i>CASE 2 (Over-run Operation)</i>	Stress (MPa)	1077	1127	4.64 %
	Displacement (mm)	0.314	0.336	7.01 %
<i>CASE 3</i>	Stress (MPa)	716	761	6.30 %
	Displacement (mm)	0.211	0.215	1.90 %
<i>CASE 4</i>	Stress (MPa)	846	898	6.15 %
	Displacement (mm)	0.242	0.251	3.72 %

The 2-D solution is obtained in six times less CPU time than 3-D model. Similarly, the number of nodes and elements are more than 10 times less than that of 3-D model. The results clearly show that the 2-D approximation technique predicts the displacement and stresses of the LP turbine very accurately and in much less CPU time.

Conclusion

Computational stress analysis of low pressure turbine of a small turbofan engine was performed using 2-D approximation technique developed by authors. The results of this analysis was compared with the another stress analyses of the same geometry modeled with 3-D finite elements. It was observed that the results are within 10% of each other. 2-D finite element results were considered better as they were obtained using much less computational resources.

Acknowledgement

Authors acknowledge Mr. Faisal Siddiqui and Mr. Shahzad Saleem, graduate students at College of Aeronautical Engineering, NUST, Pakistan, for their help in addressing modeling and FEM problems using ANSYS® software. Also we are thankful to Sijal Ahmed, Visiting Engineer at College of Aeronautical Engineering, NUST, Pakistan, for his help in developing the CAD model.

References

- [1] C.T.F. Ross (1985) Finite Element Methods in Structural Mechanics, John Wiley and Sons Inc., New York, USA.
- [2] Robert D. Cook (1981) Concepts and Application of Finite Element Analysis, 2nd Edition, John Wiley and Sons Inc., New York, USA.
- [3] V. Ramamurti, D. A. Subramani and K. Sridhara (1998) J. of Mech. Mach. Theory 30, 619-628.
- [4] Khan, A. M., Ahmed, M. N., and Mushtaq, S., (2006) J. of Eng. & App. Sc. 25, 47-55
- [5] ANSYS® Version 9.0 Verification Manuals, (2004), SAS IP Inc.
- [6] Material Handbook of High Performance Alloys, Special Metals Corp (2001).

A Parametric Study of Deformations and Stresses in Pin-loaded Tubes under Axial Tension

Ishtiaq Ahmad ¹

Abstract

This paper describes the main results of an experimental study of deformations and stresses developed in pin-loaded tubes under axial tension. The results of 28 pin-tube configurations, obtained using stress-freezing technique of 3-dimensional photoelasticity, have been presented. The parameters studied include; (a) pin/tube diameter ratio, (b) the position of the pin axis relative to the tube end, (c) tube thickness/diameter ratio (d) lubrication at the pin-tube interface, (e) pin stiffness, (f) pin clearance in the pin-hole and (g) some alternate modes of tensile loadings. The data provides a useful reference in the design of a pin-loaded tube under axial tension.

Keywords: Pin-Loaded Tubes, Axial Tension, Tube Deformations, Stress Indices

Introduction

Pinned connections in plates (or lugs) and tubes are a common feature in a wide range of engineering applications. Grant and Smart [1] has reported the extensive use of pin-loaded tube as a form of connection in the aircraft industry. The stress state in such a tube is therefore of considerable importance. However, the literature review by the author [2] reveals that much previous work has been devoted to the stress analysis of cylindrical tubes with empty transverse holes and of 2-dimensional problems in the form of pin-loaded plates and lugs. This paper describes a part of the results of a systematic parametric study, using stress-freezing technique of 3-dimensional photoelasticity, of the stresses and deformations in pin-loaded tubes. Some of the results of the experimental investigations of the author regarding deformations and stresses in pin-loaded tubes have been published elsewhere [3, 4, 5, and 6].

Model Design and Manufacture

A typical pin-tube configuration is shown in Fig. 1 which also shows the symbols and notations. Each photo elastic model incorporated two separate configurations, one at each end, designated L for lower and U for upper for ease of reference. The defining values of dimensionless parameters d/D , h/D and t/D for each configuration presented in this paper are listed in Table 1. Each configuration of Table 1 has been assigned the same reference number as was assigned in the publication [2] where full coverage of the detailed photo elastic investigation of stresses in pin loaded tubes have been reported.

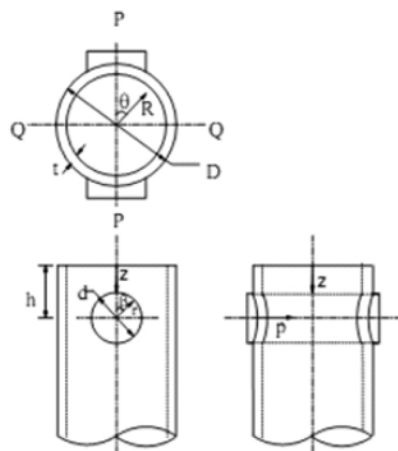


Figure 1: Symbols and notations of a pin-loaded tube

¹Pakistan Institute of Engineering and Applied Sciences, Nilore, Islamabad

The pin-tube interface was lubricated for 13U configuration while pin-tube interface remained un-lubricated for the rest of the configurations presented in this paper. Except for 18U (a configuration designed for the study of effect of pin clearance) the fit of the pin in the tube holes was 'snug' i.e. there was neither clearance nor interference. The effect of variation of d/D have been studied using 0.10, 0.20, 0.40 and 0.60 as the values of d/D while four values of h/D (i.e. 0.50, 1.00, 1.50 and 2.00) have been used for studying the effect of h/D . The values of t/D presented in this paper, for studying the effect of variation of tube thickness, are 0.04, 0.08, 0.16, 0.25 and 0.32

Each model was machined from a casting of Araldite CT200 (with hardener HT 901), with annealing after an initial 'rough' machining prior to final machining. The outer dimension D of each model was 50.0 mm. The length of each model presented in this paper was 350 mm (i.e. $7D$). With this length and for h/D values included in the model series the two ends of the model could be regarded as independent.

The standard form of pin consisted of Araldite sleeve on a cylindrical steel core-piece. This form of pin provided an Araldite/Araldite contact at the pin-tube interfaces and adequate pin stiffness under the applied load. The core-piece of 14U configuration was aluminum alloy (reducing the pin stiffness by a factor of 3).

Experimental Procedures

The models were subjected to the stress-freezing cycle in a temperature-controlled oven. Tensile load was applied axially at pin-center (see Fig. 2a) for all configurations except for model 19 (see Fig. 2b), model 20 (See fig 2c) and model 21 (see fig 2d)

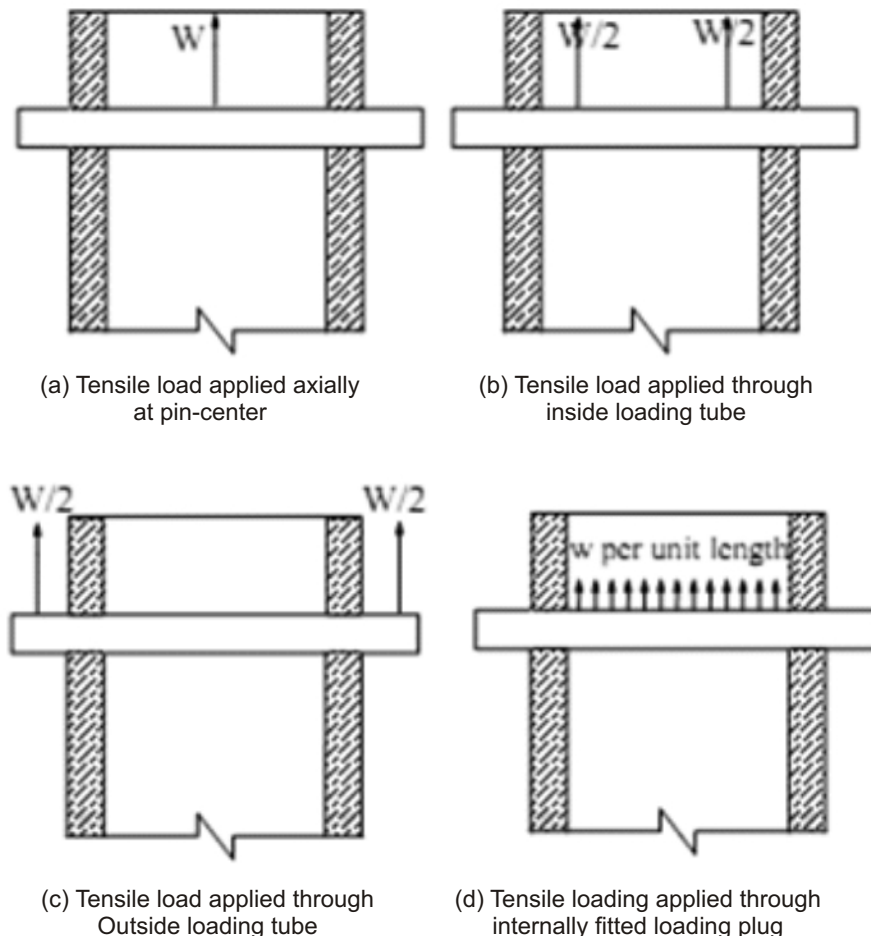


Figure 2: Schematics of alternate modes of tensile loading

After completion of the stress-freezing cycle, the principal diameters of the stress-frozen tube were measured at suitably spaced positions in the two planes of symmetry (i.e. planes PP and QQ; see Fig. 1). The tube was then cut into two halves along two axial lines with θ coordinates (see Fig. 1) of 120° and 300° and the ‘through-thickness’ isochromatic fringe patterns around each hole was photographed. Before slicing some ‘through thickness’ isochromatic fringe readings were also taken. A diffused light polariscope was used for taking isochromatic fringe order readings; fractional orders were obtained by use of tardy compensation technique.

For presentation purposes, all stresses were expressed in the form of stress indices obtained by dividing values of the fringe order per unit thickness by the average ‘through- thickness’ fringe order per unit thickness, N_{ref} , obtained from readings taken around the tube at about the mid-length position where the stresses were almost uniform. [For the thicker models (namely, models 8 and 9) the material fringe value of the model material was obtained from a tensile calibration specimen and the required N_{ref} value was calculated using the stress-optic law.] Derived stress indices are denoted by the symbol I with the subscripts z , or β , as appropriate, and an additional subscript i or o to denote the inner or outer surface.

Results and Discussion

The main results of maximum deformations and stresses for 28 pin-tube configurations, with tensile loading, are tabulated in Table 1. The general pattern of tube deformations and the distribution of tangential stresses around pin-hole have been presented (in Figs 3 and 4) for the pin-tube configuration 12U [2] having d/D , h/D and t/D as 0.2, 1.0 and 0.08 respectively model are exemplified in Fig.3, where the quantity $\Delta D/DW$ (W being the applied load) is plotted for the configuration 12U against the non-dimensional axial coordinate.

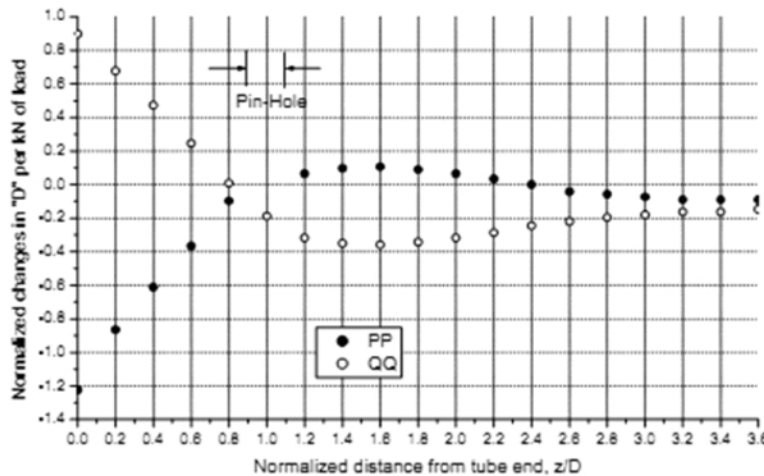


Figure 3: Tube deformations of configuration 12U

Table 1: main result of maximum deformations and stresses for some tensile loaded pin-tube configurations

Pin-Tube Configuration		Ref. No.	$\Delta D_{max}(PP)/DW$ $kN^{-1}(at\ z/D)$	$\Delta D_{max}(QQ)/DW$ $kN^{-1}(at\ z/D)$	$I_{z}(PP)$ max	$I_{\beta o}$ max around pin-hole (β_{max}) degree
(d/D,h/D,t/D), any other variable						
Study of effect of variation of d/D and h/D while other parameters are fixed						
(0.1,0.5,0.08)	15U		-1.33 (0)	0.83 (0)	-22.79	16.78 (82°)
(0.1,1.0,0.08)	5 U		-0.85 (0)	0.59 (0)	-13.78	15.74 (75°)
(0.2,0.5,0.08)	11U		-1.37 (0)	0.92 (0)	-15.92	12.87 (90°)
(0.2,1.0,0.08)	12U		-1.22 (0)	0.90 (0)	-11.10	11.34 (90°)
(0.2,1.5,0.08)	4 U		-0.40 (0)	0.25 (0)	-7.70	10.33 (75°)
(0.2,2.0,0.08)	3U		-0.25 (1.2)	0.24 (1.0)	-7.50	9.90 (86°)
(0.4,0.5,0.08)	3 L		-1.31 (0)	0.94 (0)	-5.33	10.75 (90°)
(0.4,1.0,0.08)	16U		-1.33 (0)	1.06 (0)	-5.47	8.88 (90°)
(0.4,2.0,0.08)	17L		-0.33 (1.0)	0.28 (1.0)	-4.19	8.03 (85°)
(0.6,1.0,0.08)	4 L		-1.58 (0)	1.29 (0)	-4.03	7.47 (90°)
(0.6,1.5,0.08)	5 L		-0.73 (0)	0.45 (0.2)	No results	6.66 (90°)

Effect of variation of t/D studied for two configurations of d/D and h/D keeping other parameters fixed					
(0.4,1.0,0.04)	6 L	-7.25 (0)	5.08 (0)	-6.99	10.02 (90°)
(0.4,1.0,0.08)	16U	-1.33 (0)	1.06 (0)	-5.47	8.88 (90°)
(0.4,1.0,0.16)	7 L	-0.189 (0)	0.145 (0)	-3.95	7.65 (87°)
(0.4,1.0,0.25)	8 L	-0.046 (0)	-0.043 (1.0)	-3.70	5.87 (90°)
(0.4,1.0,0.32)	9 L	-0.039 (0)	-0.037 (1.0)	-3.52	4.81 (87°)
(0.2,0.5,0.04)	6 U	-5.65 (0)	3.11 (0)	-17.72	14.22 (83°)
(0.2,0.5,0.08)	11U	-1.37 (0)	0.92 (0)	-15.92	12.87 (90°)
(0.2,0.5,0.16)	7 U	-0.263 (0)	0.215 (0)	-9.76	11.66 (80°)
(0.2,0.5,0.25)	8 U	-0.067 (0)	0.046 (0)	-8.27	7.01 (75°)
(0.2,0.5,0.32)	9 U	-0.055 (0)	0.031 (0)	-6.25	6.80 (83°)
Study of effect of lubrication and pin stiffness keeping other parameters fixed					
(0.2,1.0,0.08)	12U	-1.22 (0)	0.90 (0)	-11.10	11.34 (90°)
(0.2,1.0,0.08), lubricated pin	13U	-1.22 (0)	0.84 (0)	-10.89	11.03 (85°)
(0.2,1.0,0.08), less stiff pin	14U	-1.22 (0)	0.891 (0)	-11.91	11.93 (87°)
Study of effect of clearance between pin-hole and pin keeping other parameters fixed					
(0.2,0.5,0.08)	11U	-1.37 (0)	0.92 (0)	-15.92	12.87 (90°)
(0.2,0.5,0.08), d-d _p =0.25mm	18U	-1.39 (0)	0.951 (0)	-16.81	14.37 (75°)
Effect of variation of mode of tensile loading studied for two configurations of d/D and h/D keeping other parameters fixed					

- ¹ load applied axially at pin centre.
- ² loads applied through inside loading tube.
- ³ load applied through outside loading tube.
- ⁴ load applied through internally fitted loading plug.

As evident from Fig.3, above the pin-hole [the words ‘above’ and ‘below’ are used here in the sense implied in Fig. 1, regardless of whether the hole is at the upper end of the model (U) or the lower (L)] the diameter changes in the PP plane, ΔD(PP), were negative, while those in the QQ plane,

(0.4,1.0,0.08) ¹	16U	-1.33 (0)	1.06 (0)	-5.47	8.88 (90°)
(0.4,1.0,0.08) ²	19L	-0.945 (0)	0.834 (0)	-6.52	8.83 (90°)
(0.4,1.0,0.08) ³	20L	-1.17 (0)	1.01 (0)	-6.65	8.96 (90°)
(0.4,1.0,0.08) ⁴	21L	-0.124 (0)	-0.141 (1.0)	-4.03	5.20 (90°)
(0.2,0.5,0.08) ¹	11U	-1.37 (0)	0.92 (0)	-15.92	12.87 (90°)
(0.2,0.5,0.08) ²	19U	-0.796 (0)	0.756 (0)	-15.59	13.17 (90°)
(0.2,0.5,0.08) ³	20U	-1.24 (0)	0.885 (0)	-15.33	13.03 (90°)
(0.2,0.5,0.08) ⁴	21U	-0.124 (0)	-0.116 (1.2)	-7.63	9.37 (90°)

ΔD(QQ), were positive. Close to the pin-hole ΔD(QQ) decreases to zero. Below the pin-hole ΔD(PP) is positive and ΔD(QQ) is negative. These deformations increase to secondary maxima just below the lower edge of the pin-hole and then decrease over a length of the order of one tube diameter until the cross section shows a small uniform reduction in diameter. A number of conclusions can be drawn from the tabulated data:

1. The maxima of tube deformations generally occurred at the open end of the tube. The maximum deformation values occurred at z/D other than zero (0.2 to 1.2) for thinner models having h/D ≥ 1.50 (3U, 5L) or loaded through internally fitted loading plugs (21L, 21U) and for thicker models having t/D ≥ 0.25 (8L, 9L).
2. With the only exception of 21L (a configuration loaded using an internally fitted plug) The absolute value of maximum diameter change in the PP plane was always greater than that in the QQ plane.
3. Within the limits of the experimental error it can be generalized that for a given d/D Value, maximum deformations tend to decrease with increasing h/D. This conclusion is in line with the findings of Grant and Smart [1].

4. Within the limits of the experimental error it can be generalized that for a given h/D Value, maximum deformations tend to increase with increasing d/D .
5. Rapid decrease in deformations has been observed with increasing t/D . This conclusion is in line with the findings of Grant and Smart [1]. Tendency of change of sign for the maximum values of $\Delta D(QQ)/DW$ has been observed for thicker models (8L, 9L) and for the model loaded through internally fitted loading plug(21L, 21U).
6. Practically model deformations remained unaffected by the lubrication of pin-tube Interface, change of pin stiffness and the introduction of clearance between pin-hole and pin.
7. The modes of tensile loading can be arranged in the order of increasing maximum deformations as: loading through internally fitted loading plug (minimum deformations), load applied through inside loading tubes, load applied through outside loading tube and load applied axially at pin centre (maximum deformations).

Maximum compressive axial surface stress in the PP plane occurred at the inner surface immediately above the pin-hole. These maximum values are shown, in table 1, in the form of non-dimensional stress index $I_{zi}(PP)_{max}$. It can be seen from the tabulated data that:

1. With the only exception of configurations 3L and 16U, for a given d/D value, $I_{zi}(PP)_{max}$ tend to decrease with increasing h/D .
2. For a given h/D value $I_{zi}(PP)_{max}$ decreases with increasing d/D .
3. $I_{zi}(PP)_{max}$ decreases with increasing t/D .
4. The use of clearance fit pin and less stiff pin resulted in increase of the value of $I_{zi}(PP)_{max}$ while lubricating pin-tube contact has resulted in slightly reducing this value.
5. Among various modes of tensile loading least value of $I_{zi}(PP)_{max}$ was observed for the tensile loading applied through internally fitted loading plug.

Tangential Stress Indices around the Pin-holes

The general distribution of tangential stress indices, at inner and outer surfaces of the pin-holes, is illustrated in Fig. 4, using the data of configuration 12U. The prominent general features of the distribution of tangential stress index around pin-holes include the following.

1. Almost without exception the outer edge value was greater (algebraically) than the inner edge value for all β .
2. The maximum stress index always occurred at the outer edge at β values ranging from 75 to 90 degrees (see Fig.1).
3. At $\beta = 0$ (the centre of pin-tube contact arc) the tangential stress indices for both inner and outer surfaces are positive.
4. Sign of tangential stress, especially at the inner surface, is negative for a small arc (the length of which increases with increasing d/D and is centered on $\beta = 180^\circ$).

It can be seen from the tabulated values that:

1. For a given d/D value, $I_{\beta o} \max$ decreases with increasing h/D .
2. For a given h/D value, $I_{\beta o} \max$ decreases with increasing d/D .
3. $I_{\beta o} \max$ decreases with increasing t/D .

4. Lubrication resulted in slight reduction while the use of less stiff pin and the introduction of clearance resulted in increasing $I\beta_0$ max.
5. Among various modes of tensile loading least value of $I\beta_0$ max was observed for the tensile loading applied through internally fitted loading plug.

Optimum Design Parameters

With a view of having minimum tube deformations and reducing stresses around pin-holes (in case the trends of variation of deformations and stresses are opposite to each other following recommendations are based on the consideration of reduction in the stresses) following recommendations are made for the optimum design of pin-loaded tubes under axial tension.

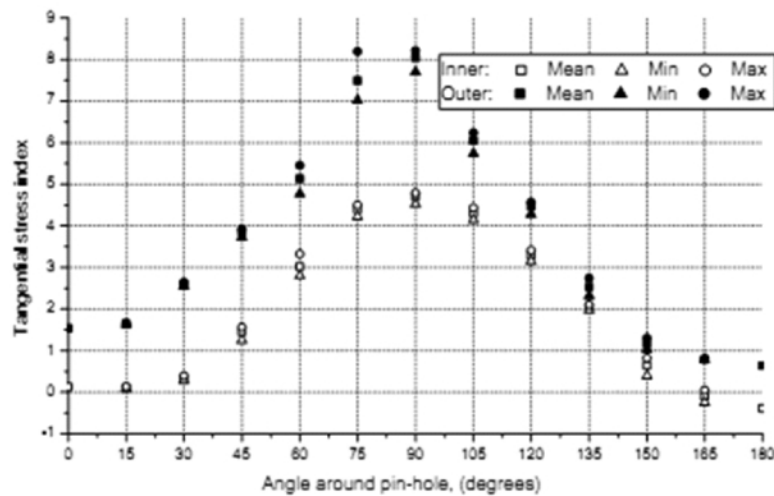


Figure 4: Tangential stress indices around pin-hole of configuration 12U

1. Increasing h/D is beneficial; however increase of h/D beyond 1.5 does not produce significant reduction in tube deformations and the stresses around pin-hole.
2. Increasing d/D is beneficial; however increase of d/D beyond 0.4 does not produce significant reduction of the stresses around pin-hole.
3. Within the limits of restrictions of self weight it is recommended to increase t/D .
4. With reference to the reduction of stresses around pin-holes it is recommended to lubricate the pin, increase pin stiffness and avoid the use of clearance-fit pin.
5. Application of load through an internally fitted loading plug is recommended for minimizing tube deformations and the stresses around pin-hole.

References

- [1] Grant, R. J., Smart, J. (1997) *J. Strain Analysis*, 32, 213-228.
- [2] Ahmad, I. (1994) *Stresses in pin-loaded tubes*. PhD thesis, University of Manchester.
- [3] Ahmad, I., Stanley, P. (1994) 'In: Proc. 10th Int. Conf. on Experimental Mechanics, Lisbon, pp.137-142, Silva Gomes, J.F., Branco, F.B. (Eds) A. A. Balkema, Rotterdam, Brookfield.
- [4] Stanley, P., Ahmad, I. (1998) 'In: Proc. 11th Int. Conf. on Experimental Mechanics, Oxford, pp. 89-94, Allison, I.M. (Ed.), A. A. Balkema, Rotterdam, Brookfield.
- [5] Ahmad, I., Stanley, P. (2000) *J. Strain Analysis*, 35, 329-345.
- [6] Ahmad, I., Stanley, P. (2001) *J. Strain Analysis*, 36, 35-49.

Development of Novel Method for the Selection of Material for Axial Flow Compressor Blade

M. Javed Hyder¹ and M. Omair Khan²

Abstract

A novel method has been devised for the selection of material for axial flow compressor base on the centrifugal stresses generated at the root of the blade of first stage. The centrifugal stress limits the blade tip speed which in turn depends on the rotational speed, blade material and height of the blade. At present the blade tip velocity used is 350 m/sec. It is shown that for a safety factor of 2 or greater the suitable material are found to be Aluminum Alloy 7075-T6, Aluminum Alloy 2024-T4, Carbon and Alloy Steel 52100 A (Annealed), Magnesium Alloy HK31XA-H24 and Carbon and Alloy Steel 4340 HR (Heat Treated). Also the dependency of the root and tip radius of the blade on material and safety factor is presented.

Keywords: Novel Method, Axial Flow, Flow Compressor Blade

Introduction

To reduce specific fuel consumption high overall pressure ratio is required in gas turbines. Axial flow compressors provide both higher pressure ratio and higher efficiency as compared to the centrifugal compressor. Earlier axial flow units had pressure ratio of around 5:1 and it required about 10 stages. Over the years the pressure ratio has exceeded 40:1 and the numbers of stages have been reduced resulting in drastic reduction in weight of gas turbine [1].

The super alloys consists of alloys of iron-nickel-, nickel-, and cobalt base that are destined generally for use above about 540°C (1000°F) [2]. Since the compressors outlet temperature is below this temperature conventional alloys can be used [1].

The centrifugal stress in the rotor blade depends on the rotational speed, the blade material and the length of the blade. The maximum centrifugal tensile stress (σ_{max}) which occurs at the All blade root is found to be [1]:

$$\sigma_{max} = \frac{\rho_b U_t^2}{2} \left[1 - \left(\frac{r_r}{r_t} \right)^2 \right] \quad (1)$$

It shows that the stress is proportional to the density (ρ_b) of the blade material and the blade tip speed (U_t). Hub to tip ratio of the radius (r_r/r_t) also effect the stresses created due to centrifugal forces. Generally hub to tip ratio is taken to be 0.5 at the first stage. Incorporating the factor of safety n , along with the ultimate tensile strength (σ_{uts}), (see table 1) of the material used then the blade tip speed is given by:

$$U_t = \sqrt{\frac{\sigma_{uts}}{\rho_b 0.375 n}} \quad (2)$$

It gives maximum limit of the blade tip speed which that material can tolerate with out failure. It can be noted that the density of the material is inversely proportional to the blade tip velocity. But it is directly proportional to the ultimate tensile strength.

Blade tip velocity plays a very critical role in compressor design. First stage blade height is directly influenced by the blade tip speed since it has the largest height as compared to the subsequent stages. Blade tip speed is related to the rotational speed (N) by:

^{1&2} Department of Mechanical Engineering, PIEAS, Islamabad.

$$U_t = 2\pi r_t N \quad (3)$$

There is no equation which enables the designer to select a suitable value of rotational speed. However by assuming values for the blade tip speed and axial velocity and the hub to tip ratio at inlet of the first stage rotational speed can be found. Using the above equations effect of material density, material strength and blade tip speed on safety factor is shown in figure-1. The material properties given in the table-1 is used [3]. It clearly shows that for a given safety factor (say 2.5) maximum blade tip velocity is limited to 175 m/s for copper alloy 80-20 but for carbon alloy steel the tip speed may be raised to 375 m/s whereas for aluminum alloy 7075-T6 the limiting value is about 475 m/s.

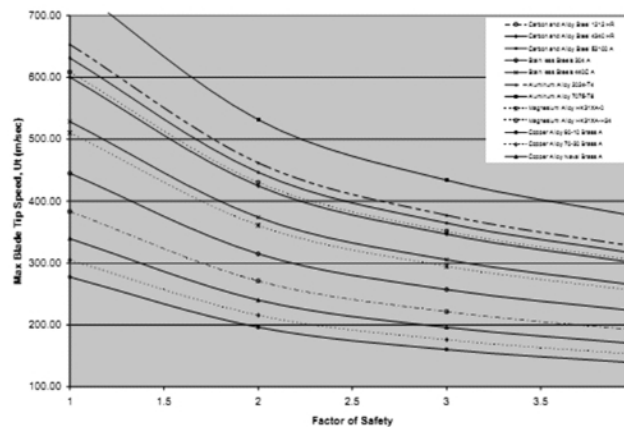


Figure 1: Behavior of blade tip speed and safety factor for various materials

The experience suggests that a tip speed of 350 m/s is used [1]. L. M. Larosiliere et al [4] has shown that with advance aerodynamic design per stage pressure ratio can be increased to 5.0 and the blade tip speed can be used as high as 550 m/s. Hence for a safety factor of 2.5 to have a tip speed greater than 350 m/s the material that can be used are listed below. The most preferred material is listed first.

1. Aluminum Alloy 7075-T6
2. Aluminum alloy 2024-T4
3. Carbon and Alloy Steel 52100 A
4. Magnesium Alloy HK31XA-H24
5. Carbon and Alloy Steel 4340 HR

It can be seen that Aluminum alloy 7075-T6 and Aluminum alloy 2024-T4 has ultimate tensile strength of 593 MPa and 448 MPa respectively with the density of 2.8 Mg/m³. These alloys don't have ultimate tensile strength as high as carbon-steel alloy 52100 A (annealed), with ultimate tensile strength of 1151 MPa and density 7.7 MPa but these Aluminum alloys are lighter than later alloy thus resulting in better choice for compressor blade design in view of centrifugal forces. The other mentionable alloy is the Magnesium alloy HK31XA-H24 having the ultimate tensile strength of 250 MPa and density of 1.8 Mg/m³ here too the density is having a dominant effect on the blade tip speed and thus on the centrifugal stress.

If the value of rotational speed 250 rps (15000 rpm) is used then the tip radius can be evaluated using equation 3 for any value of blade tip speed which can be taken from the figure 1 corresponding to the selected safety factor. In the figures from 2 to 6 the variation of radius for different safety factors is shown. It can be seen that as the safety factor is increased the both the tip and root radii are decreasing which is obvious from figure 1, since the increase in safety factor reduces the maximum blade tip speed. At the same time the as the safety factor is reduced the gap between the two curves is reduced which represents the blade height. So by increasing the safety factor the blade height is also decreasing.

Table 1: Material properties of various materials [3]

S.r No.	Alloys	Heat Treatment	Ultimate Tensile Strength σ_{ut} Mpa	Young's Modulus E Mpa	Density ρ Mg/cubic. m
1	Aluminum Alloy 7075-T6		593	538	2.8
2	Aluminum Alloy 2024-T4		448	296	2.8
3	Carbon and Alloy Steel 52100 A	Annealed	1151	903	7.7
4	Magnesium Alloy HK31XA-H24		250	214	1.8
5	Carbon and Alloy Steel 4340 HR	Hot rolled	1041	910	7.7
6	Stain less Steels 440C A	Annealed	807	462	7.7
7	Magnesium Alloy HK31XA-0		176	131	1.8
8	Aluminum Alloy 7075-0		234	99	2.8
9	Carbon and Alloy Steel 1045 HR	Hot rolled	638	414	7.7
10	Stain less Steels 302 A	Annealed	634	234	7.7
11	Stain less Steels 303 A	Annealed	600	241	7.7
12	Stain less Steels 304 A	Annealed	572	276	7.7
13	Carbon and Alloy Steel 1020 HR	Hot rolled	455	290	7.7
14	Carbon and Alloy Steel 1212 HR	Hot rolled	424	193	7.7
15	Carbon and Alloy Steel 1018 A	Annealed	341	221	7.7
16	Copper Alloy Naval Brass A	Annealed	376	117	8.7
17	Carbon and Alloy Steel 1010 A	Annealed	303	200	7.7
18	Carbon and Alloy Steel 1002 A	Annealed	290	131	7.7
19	Copper Alloy 70-30 Brass A	Annealed	303	72	8.7
20	Aluminum Alloy 1100-0		83	31	2.8
21	Copper Alloy 90-10 Brass A	Annealed	251	58	8.7
22	Copper Alloy 80-20 Brass A	Annealed	247	50	8.7

If the value of rotational speed 250 rps (15000 rpm) is used then the tip radius can be evaluated using equation 3 for any value of blade tip speed which can be taken from the figure 1 corresponding to the selected safety factor. In the figures from 2 to 6 the variation of radius for different safety factors is shown. It can be seen that as the safety factor is increased the both the tip and root radii are decreasing which is obvious from figure 1, since the increase in safety factor reduces the maximum blade tip speed. At the same time the as the safety factor is reduced the gap between the two curves is reduced which represents the blade height. So by increasing the safety factor the blade height is also decreasing.

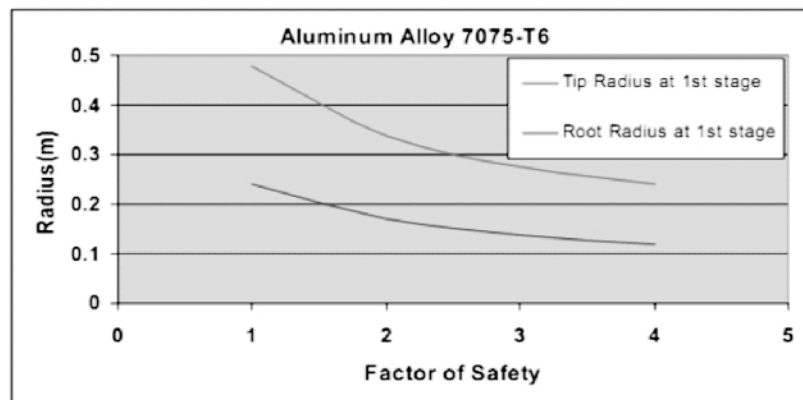


Figure 2: Effect of safety factor on root and tip radius of Aluminum alloy 7075-T6 compressor blade

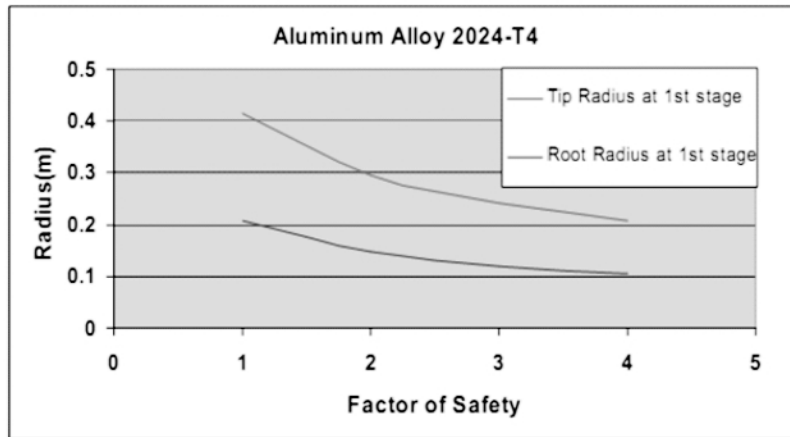


Figure 3: Effect of safety factor on root and tip radius of Aluminum alloy 2024-T4 compressor blade

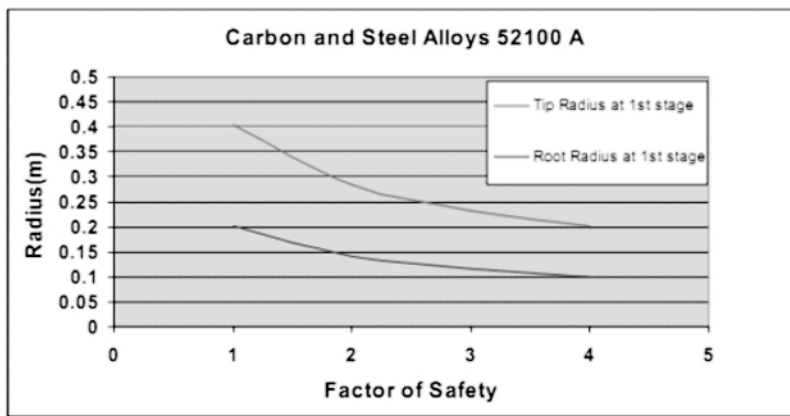


Figure 4: Effect of safety factor on root and tip radius of Carbon and Steel alloy 52100 A compressor blade

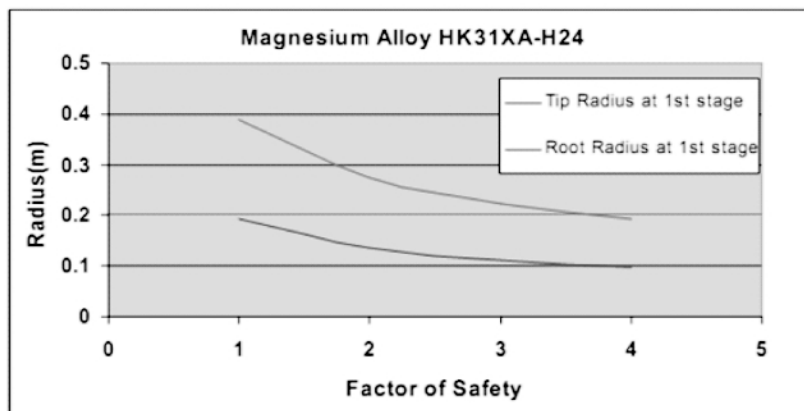


Figure 5: Effect of safety factor on root and tip radius of Magnesium alloy HK31XA-H24 compressor blade

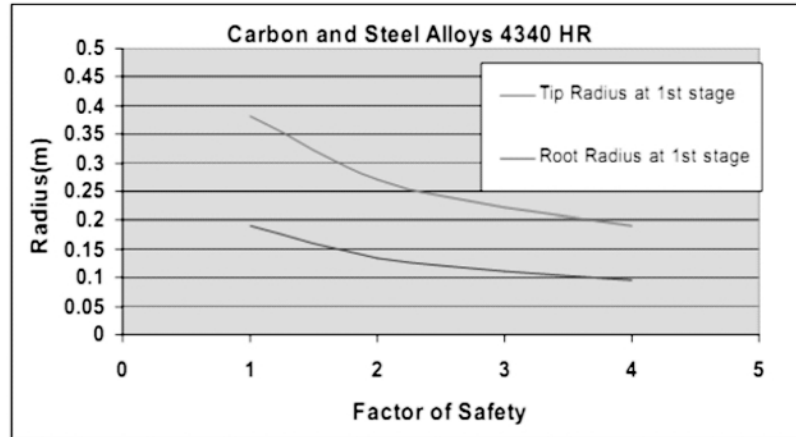


Figure 6: Effect of safety factor on root and tip radius of Carbon and Steel alloy 4340 HR compressor blade

References

- [1] H.H. Saravanamuttoo, G.F.C. Rogers, and H. Cohen, Gas turbine theory, 5th edition, Pearson education series.
- [2] Matthew J. Donachie and Stephen J. Dionachie, Super Alloys: A technical Guide, 2nd edition.
- [3] Robert C. Juvinall and Kurt M. Marshek, Fundamentals of Machine Component Design, 4th edition, John Wiley & Sons, Inc.
- [4] Louis M. Larosilere, Jerry R. Wood, Michael D. Hathaway, Adam J. Medd and Thong Q. Dang, Aerodynamic Design Study of Advance Multistage Axial Compressor, NASA/TP-2002-211568, December 2002.

Effects of Cutting Parameters in Erosion Failure of Ductile Materials in Abrasive Water Jet Machining

Asif Iqbal, Naeem Ullah Dar¹ and Mubasher Chohan²

Abstract

Abrasive water jet (AWJ) cutting is versatile most of all the metal cutting processes as its applicability is not marred by the kind of material to be cut. The main mechanism of cutting involved is the erosion of material matrix, which is impinged by high velocity particles of abrasive material mixed in narrow stream of water. Erosion phenomenon for ductile materials is different as compared to that of brittle materials. Ductile erosion is defined as a cutting process in which the abrasive particles progressively cut or gouge the eroded materials. Brittle erosion is described as a cracking process in which material is removed by the propagation and intersection of cracks ahead of the abrasive particle. In this study the effects of different cutting parameters, namely: jet pressure, cutting speed, material's hardness, and abrasive quantities were investigated, experimentally, upon a ductile material. Experiments were performed upon hot work tool steel AISI H13, hardened to two different values: 39HRc and 49HRc. It was observed that the erosion process could be divided into two categories: an upper smooth zone which is free of any striations and its primary surface irregularity is roughness, and a lower rough zone where the wavy striations are the dominant characteristic features. It was found that cutting speed, jet pressure, and material hardness were the influential parameters upon arithmetic surface roughness of striation free zone. It was also observed that low cutting speed and high jet pressure gave larger proportion of striation free area, while the effect of abrasive quantity was insignificant.

Keywords: Erosion, Ductile Materials, Abrasive Water

Introduction

Abrasive Water Jet (AWJ) Machining is a process in which a very high velocity stream of water is used to accelerate the particles of abrasive material, which, in turn cut the work piece material by making use of erosion principle. As compared to other cutting methods, AWJ cutting steers clear of the heat-affected zones and distortion created by laser and plasma-arc systems [1]. Water at pressure of up to 5000bars is pressed through the orifice of diameter 0.5 to 1mm and ultra high speed jet is obtained.

The velocity of water jet is proportional to the square root of the water pressure and usually reaches values up to 1000m/sec [2].

AWJ cutting is considered to be the most versatile material cutting process, which is not restrained by the type of material to be cut. There are two major shortcomings of AWJ cutting process that limits its wide-spread industrial application: generation of wavy striated surfaces in cutting of thick plates and high-running cost. The cut surface produced in plates can be divided into two zones: an upper smooth zone which is free of any striations and its primary surface irregularity is roughness, and a lower rough zone where the wavy striations are the dominant characteristic features [3, 4]. The authors in [5] reported that the formation of striations is a result of external disturbances such as machine vibrations. This idea, later on, could not get popularity. In [3] it was reported that wavy striation patterns are formed by the wavy abrasive particle kinetic energy distribution related to the cut surface. With respect to AWJ cutting the materials can be divided into two categories: ductile and brittle.

The mechanics of AWJ cutting of the ductile materials has been well covered by Hashish [6, 7]. He described that AWJ cutting consists of cyclic penetration process that consists of two cutting zones: cutting wear zone and deformation wear zone. The process follows Biter's erosive theory [8, 9]. In the cutting wear zone, material removal is by abrasive particles striking the work piece at shallow angles of attack while material removal in the deformation wear zone is by the abrasive particles encroaching at large angles of attack. Figure 1 shows the detail. It can, thus, be concluded from Hashish's description that material

^{1,2} Mechanical Engineering Department, University of Engineering & Technology Taxila.

removal process in ductile materials is regarded to erosion at shallow angles and plastic deformation at large angles. In [10] the authors threw light upon cutting mechanism of brittle materials. The proposed mechanism consists of micro-cutting and inter-granular fracture at shallow angles of impact followed by plastic deformation and inter-granular fracture at near-orthogonal angles of impact.

In [11, 12] it has been reported that plain water jet impinging on surface of hard materials causes insignificant material removal, thus the main purpose of water jet is to accelerate the abrasive particles in order to render them the ability to erode the material.

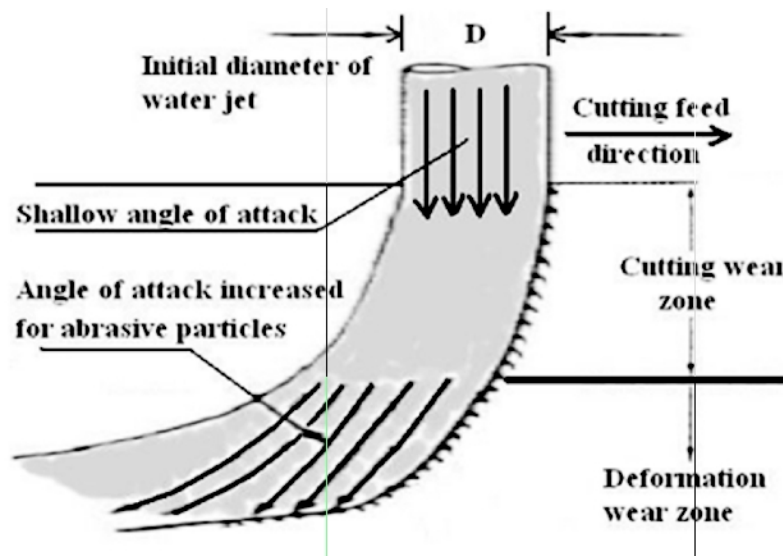


Figure 1: Cutting wear zone and deformation wear zone in AWJ cutting

In few papers the technique of oscillating the nozzle head has been described and advantages like reduction in striation effects and reduction in abrasive contamination in ductile materials have been reported [4, 13, 14, 15].

Few papers have also put forward the modeling approach of AWJ cutting process. Two papers, [10, 16], present the analytical models for AWJ cutting process of ductile and brittle materials respectively, along with experimental verification. The information regarding generalized kerfs shape has been utilized to develop model for total depth of cut, which takes into account the variation in width of cut along the depth. The basic material property that determines the total depth of cut appears to be the melting specific energy rather than the elastic modulus. In [17] a model for predicting the shape of the cut profile in industrial cutting processes has been developed and applied to AWJ cutting. In [2] finite element method has been utilized in order to analyze the influence of abrasive particles rotation on the work piece material erosion in AWJ process.

The literature survey puts forward that both analytical and experimental analyses have been performed in order to investigate the AWJ cutting process, but on the other hand, the statistical analysis, including ANOVA (Analysis of Variance), and numerical optimization, has not been widely applied in this domain. In this paper the effects of four parameters, namely: material's hardness, water jet pressure, abrasive mixing rate, and cutting speed will be analyzed, experimentally, upon surface finish of cutting wear zone, and depth of striation-free zone of a ductile material. Upon experimental data, ANOVA will be performed to determine the significance of effect of each parameter. Based upon the ANOVA results, multi-criteria numerical optimization will be performed in order to determine the optimal values of the parameters which could maximize the combination of surface finish, depth of cutting wear zone, dimensional accuracy, and material removal rate, as per assigned priority levels.

Experimental Work

For this study a ductile material, AISI H13 - a chromium type, hot work tool steel - hardened to values of 39HRc and 49HRc. A four factor, two-level, full-factorial design of experiments (24 = 16 tests) was developed for investigation of two response variables. Table 1 presents detail of levels selected for each parameter (predictor variable).

Following is the description of response variables (performance measures) to be measured in 16 tests:

1. Average of arithmetic surface roughness measured at striation free zone of cut surface (R_a) - to be measured in microns.
2. Percentage proportion of striation free area (cutting wear zone) in the cut surface (P_{cwz}).

This is to be mentioned that the predictor variable V_f is also involved in a response variable called material removal rate (= Cutting feed \times Sheet thickness) - measured in mm^2 . For the industrial application of AWJ cutting the rate of production in terms of material removal rate needs to be maximized.

Level	Hardness (H) (HRc)	Jet Pressure (P) (bars)	Abrasive Mixing Rate (a_r) (g/min)	Cutting Speed (V_c) (mm/min)
1	39	2800	110	15
2	49	3600	220	30

Table 1: High and low setting of predictor variables for each material

Experimental Setup

All the 16 experiments were performed upon Bystronic ByJet 4022 Water Jet Cutting Machine, having maximum jet pressure of 4000bars. In all the tests the abrasive used was Garnet of grade 80 mesh, nozzle diameter was 1.25mm, stand-off distance was 1mm, and dimensions of work piece material to be cut were 200mm \times 200mm \times 45mm. Arithmetic surface roughness (R_a) of material cut was measured by Mahr Perthometer M1.

Experimental Results

Table 2: presents the results obtained from 16 tests

Test No.	H (HRc)	P (bars)	a_r (g/min)	V_c (mm/min)	R_a (μm)	P_{cwz} (%)
1	39	2800	110	15	3.05	55
2	39	2800	110	30	4.705	32
3	39	2800	220	15	2.93	86
4	39	2800	220	30	5.07	42
5	39	3600	110	15	2.41	100
6	39	3600	110	30	4.11	88
7	39	3600	220	15	1.96	100
8	39	3600	220	30	3.93	79
9	49	2800	110	15	2.365	45
10	49	2800	110	30	3.47	21
11	49	2800	220	15	2.01	51
12	49	2800	220	30	4.19	35
13	49	3600	110	15	2.15	100
14	49	3600	110	30	3.99	78
15	49	3600	220	15	1.54	100
16	49	3600	220	30	3.51	82

Results and Discussion

The experimental data have been analyzed using ANOVA tool and numerical optimization has been performed using Derringer-Suich multi-criteria decision modeling approach, the detail of which can be read from [18]. All the statistical analysis, including ANOVA and numerical optimization, were performed using commercial statistical software called Design-Expert®.

Table 3 presents the ANOVA performed upon data related to R_a . The effects of all the individual predictor variables have been shown. The effects of all the possible interactions among the predictor variables were analyzed and only the significant interactions have been shown in the table.

Table 3: ANOVA details for R_a

Source	Sum squares	DoF	Mean square	F value	p-value	Significance
Model	16.945	10	1.694	47.734	0.0002	Significant
H	1.525	1	1.525	42.966	0.0012	Significant
P	1.097	1	1.097	30.910	0.0026	Significant
a_t	0.077	1	0.077	2.169	0.2008	Not significant
V_c	13.250	1	13.250	373.241	<0.0001	Significant
$H \times P$	0.391	1	0.391	11.004	0.0211	Significant
$P \times a_t$	0.339	1	0.339	9.558	0.0271	Significant
$a_t \times V_c$	0.240	1	0.240	6.764	0.0482	Significant

Table 4: ANOVA details for P_{cwz}

Source	Sum squares	DoF	Mean square	F value	p-value	Significance
Model	11144.75	9	1238.3	21.412	0.0007	Significant
H	306.25	1	306.3	5.295	0.0610	Not significant
P	8100	1	8100.0	140.058	<0.0001	Significant
a_t	196	1	196.0	3.389	0.1152	Not significant
V_c	2025	1	2025.0	35.014	0.0010	Significant
$P \times a_t$	272.25	1	272.3	4.707	0.0731	Not significant

Table 5: Results of multi-objective optimization of AWJ cutting

Table 4 presents the ANOVA performed upon data related to P_{cwz} . The influential parameters can be arranged in the following hierarchy of descending order of significance of effect upon percentage proportion of striation free zone: P ; V_c ; H ; and a_t . It was also found from ANOVA that effect of no interaction between any two parameters was observed as significant.

Objective(s)	Optimal settings	Predicted values
min. R_a	(for $H=39$): $P=\max$; $a_t=\max$; $V_c=\min$ (for $H=49$): $P=\max$; $a_t=\max$; $V_c=\min$	$R_a \approx 1.8$ $R_a \approx 1.5$
max. P_{cwz}	(for $H=39$): $P=\max$; $a_t=175$; $V_c=\min$ (for $H=49$): $P=\max$; $a_t=165$; $V_c=\min$	$P_{cw} \approx 100\%$ $P_{cw} \approx 100\%$
min. R_a & max. P_{cwz}	(for $H=39$): $P=3300$; $a_t=\max$; $V_c=\min$ (for $H=49$): $P=\max$; $a_t=\min$; $V_c=\max$	$R_a \approx 2.1$; $P_{cw} \approx 94\%$ $R_a \approx 1.6$; $P_{cw} \approx 98\%$
min. R_a & max. MRR	(for $H=44$): $P=\max$; $a_t=\max$; $V_c=27$	$R_a \approx 3.3$; $MRR=1216$

Numerical Optimization

The target of numerical optimization could be any simultaneous combination of following four Objectives:

1. Minimize averaged arithmetic surface roughness of striation free zone (Ra)
2. Maximize percentage proportion of striation free area (Pcw)
3. Maximize production rate by maximizing material removal rate (MRR), where MRR can be defined as product of cutting feed and sheet thickness ($MRR [mm^2/min] = Vf \times t$)

Table 5 presents the optimized values (within tested range) of the predictor variables for different combination of objectives. This is to be mentioned that for the last case, involving simultaneous accomplishment of two objectives, equal priority levels were assigned to both of them.

The Cut Surface Generated

Figure 2 shows the collection of images displaying the cut surfaces of selected work pieces. Image 1 shows the surface of the work piece which produced smallest value of Pcwz (test 10). High level of cutting speed and low level of jet pressure caused the large proportion of abrasive particles to lose the threshold K.E. level, even at upper portion of surface, and consequentially, to cause prominent striations at large angle. Images 2 (test 13) and 3 (test 7) show the cut surface which are free from striations, thanks to high jet pressure and low cutting speed. Image 4 (test 8) shows uniform straight and relatively less prominent striation pattern. The striation pattern in image 5 (test 12) is quite similar to that shown in image 1 but slightly less intense. Image 6 (test 3) shows the cut surface generated by combination of low jet pressure and low cutting speed and the result is generation of thin striations at small angle of attack.

Conclusions

The paper presented a comprehensive analysis upon effects of major AWJ cutting parameters upon surface finish and proportion of striation free area. From the discussion provided above, following imperative conclusions can be drawn.

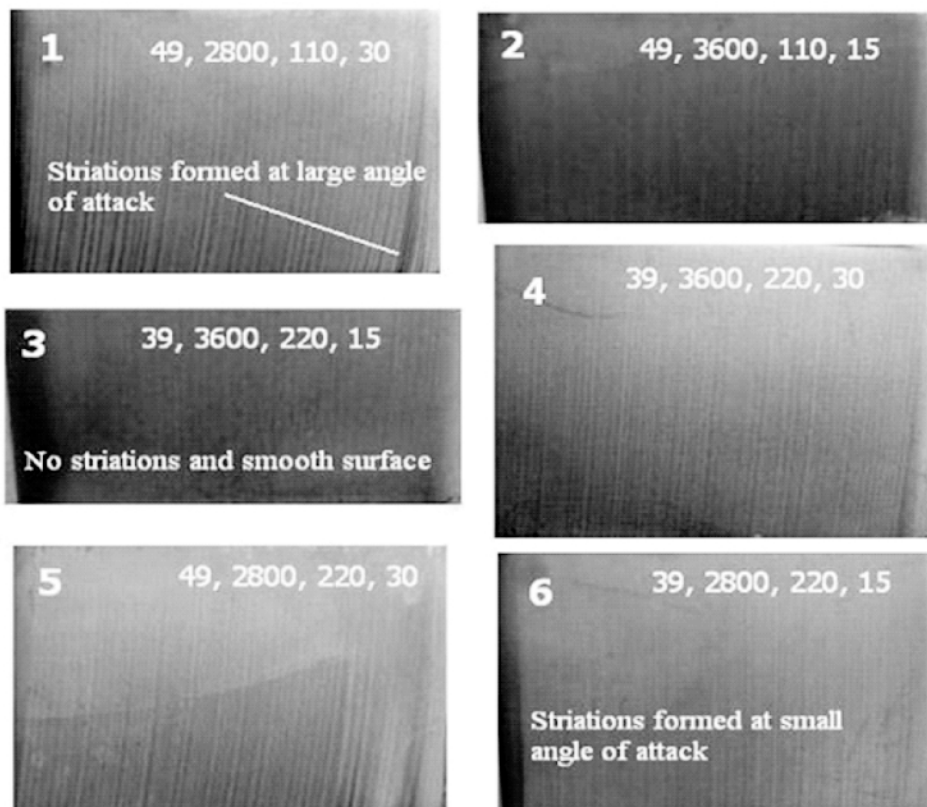


Figure 2: Cut surface generated in different test

1. Severity of striation formation is dependent upon jet pressure and cutting speed. Higher jet pressure and lower cutting speeds help to increase proportion of striation free area. The influence of cutting speed suggests that better surface texture can be obtained at the cost of productivity. The effect of abrasive mixing rate is insignificant. Increase in work piece hardness causes somewhat reduction in proportion of striation free area.
2. The surface roughness in cutting wear zone can be reduced by increasing jet pressure and reducing cutting feed.
3. AWJ cutting at low jet pressure and high cutting speed result in formation of striations at large angles of attack.

References

- [1] Jou, M. (2000). *Journal of Materials Processing Technology* 104, 17-20
- [2] Junkar, M., Jurisevic, B., Fajdiga, M., Grah, M. (2006). *International Journal of Impact Engineering* 32, 1095-1112
- [3] Chen, F.L., Siores, E. (2001). *International Journal of Machine Tools & Manufacture* 41, 1479-1486.
- [4] Lemma, E., Chen, L., Siores, E., Wang, J. (2002). *Composite Structures* 57, 297-303
- [5] Chao, J., Geskin, E.S. (1993). In: *Proceedings of the 7th American Water Jet Conference*, pp. 27-41
- [6] Hashish, M. (1984). *Journal of Engineering Materials Technology* 106, 88-100
- [7] Hashish, M. (1991). *Journal of Engineering Materials Technology* 113, 354-362
- [8] Bittar, J.G.A. (1963). *Wear* 6, 5-21
- [9] Bittar, J.G.A. (1963). *Wear* 6, 169-190
- [10] Paul, S., Hoogstrate, S.M., van Luttervelt, C.A., Kals, H.J.J. (1998). *Journal of Materials Processing Technology* 73, 206-212
- [11] Hashish, M. (1989). *Journal of Engineering Materials Technology* 111, 221-228.
- [12] Capello, E., Groppetti, R. (1993). In: *Proceedings of the 7th American Water Jet Conference*, pp. 157-174.
- [13] Chen, L., Siores, E., Morsi, Y., Yang, W. (1997). *Annals of CIRP*, 570-575
- [14] Patel, K.J. (2004). *International Journal of Machine Tools & Manufacture* 44, 1125-1132.
- [15] Wang, J. (1999). *International Journal of Advanced Manufacturing Technology* 15, 757-768.
- [16] Paul, S., Hoogstrate, S.M., van Luttervelt, C.A., Kals, H.J.J. (1998). *Journal of Materials Processing Technology* 73, 189-199.
- [17] Deam, R.T., Lemma, E., Ahmed, D.H. (2004). *Wear*, 257, 877 - 891
- [18] Derringer, G., Suich, R. (1980). *Journal of Quality Technology* 12, 214-219

Ultrasonically Assisted Turning: Finite Element Model

N. Ahmed¹, M. Abid², A.V. Mitrofanov³ and V.V.Silberschmidt⁴

Abstract

Ultrasonically assisted turning (UAT) is an advanced machining technique, where high frequency vibration (frequency $f \approx 20$ kHz, amplitude $a \approx 20$ μ m) is superimposed on the movement of a cutting tool. Compared to conventional turning (CT), this technique allows significant improvements in processing intractable materials, such as high-strength aerospace alloys, composites and ceramics. Superimposed ultrasonic vibration yields a noticeable decrease in cutting forces, as well as a superior surface finish. The current paper presents a 3D model of UAT that allows studying various 3D effects in turning, such as oblique chip formation, as well as to analyze the influence of tool geometry on process parameters, e.g. cutting forces and stresses generated in the work piece material. The FE model (based on the general FE code MSC.MARC) is used for transient, coupled thermo mechanical simulations of elasto-plastic materials under conditions of both UAT and CT. It is used to study the effect of cutting parameters and friction on UAT and CT. Also the effect of changing ultrasonic amplitude and frequency is studied. Numerical results are validated by experimental tests performed on UAT prototype.

Keywords: Ultrasonically Assisted Turning, 3D model

Introduction

Turning is a type of metal cutting where a single-point tool is used to remove unwanted material to produce a desired product, and is generally performed on a lathe machine. Modern turning techniques have been improved considerably to achieve easy machining of difficult-to-cut materials and better surface finish. Methods such as high speed turning have been in use now for considerable time. But still machining of high-strength aerospace alloys, composites and ceramics causes high tool temperatures and fast wear of cutting edges, lacks dimensional accuracy and requires a considerable amount of coolant and thus requires the development of new cutting techniques. Ultrasonically assisted turning (UAT) has proved to bring significant benefits in machining of hard-to-cut alloys. It is an advanced cutting technique, where high-frequency vibration (frequency $f \approx 20$ kHz, amplitude $a \approx 15$ mm) is superimposed on the movement of the cutting tool. Compared to conventional turning (CT), this technique allows significant improvements in processing intractable materials. A multifold decrease in cutting forces, as well as an improvement in surface finish can be achieved with the use of UAT [1].

Despite all its advantages, this technique has not yet been widely introduced in the industry. Problems such as instability of the cutting process that resulted in poor surface finish prevented the full implementation of this process. The development of an auto resonant control system [2] added stability to the system by making the vibrations regular, thus opening the way to the industrial introduction of UAT [2].

The prototype of the UAT system has been designed at Loughborough University, UK, and a program of experimental tests has been implemented confirming advantages of UAT in comparison to CT. The dynamics of UAT as a non-linear vibro-impact process was studied in [3], and the amplitude response of the cutting tool under loading was analyzed for this cutting technique.

However, thermo mechanics of the tool-work piece interaction, which is of special importance for the regime with multiple micro impacts in the process zone, and other specific features of the cutting process in UAT have not been fully understood. The finite element method (FEM) is a main computational tool for simulation of the process zone and of the tool-work piece interaction in metal cutting. A detailed review of FE models of cutting can be found in the monographs [4, 5]. In order to understand the mechanics of tool-chip interaction in UAT, and to analyze stresses and strains distributions in the cutting region, heat transfer in the work piece material and in the cutting tool and also of the cutting forces, a 2D finite-element

^{1,2} Mechanical Engineering, GIKI, Topi. NWFP, Pakistan ^{3,4} Wolfson School of Mechanical and Manufacturing, Loughborough University, UK

model was developed. An initially purely mechanical finite-element model was further improved, resulting in a transient; fully thermo mechanically coupled one for both UAT and CT. Some computational results obtained with this mode were discussed in [6].

The current paper discusses the 3D FE model of UAT that was developed as extension to the 2D model. This model allows studying various 3D effects in turning, such as oblique chip formation, as well as the influence of the tool geometry on process parameters, e.g. cutting forces and stresses generated in the work piece material.

Up to now, 3D FE models were used to simulate conventional cutting processes. The majority of the suggested schemes employ the method of chip separation along a predefined line, separating finite elements in the initial discretization of the area, hence reducing the flexibility of the analysis. Only a few schemes use other techniques, such as elements deletion based upon denetration [7], adaptive remeshing of the workpiece elements [8], and combination of both the manual deletion and remeshing [9]. Adaptive remeshing that is employed in the current paper maps calculated fields of parameters onto the new mesh to eliminate distortion in the element shapes, which could otherwise cause analysis termination. The method has an advantage of a relatively easy adjustment in the cutting direction and angles, as well as other cutting parameters, such as the feed rate, without a necessity to reformulate the boundary-value problem as in the case of separation along a predefined line.

A FEA analysis of heat generation in machining of isotropic materials was conducted in [10] in order to study the effects of the convective heat transfer. A different approach, using an orthogonal FE model coupled with an analytical 3D model of cutting, was developed in [11] to predict a chip flow angle and three-dimensional forces in the tool. Another 3D model was introduced in [8] that took into account dynamic effects, thermo-mechanical coupling, constitutive damage law and contact with friction in order to study the cutting forces and plastic deformation.

With 3D modeling of CT being used for the study of tool forces and chip flow for the last two decades, this paper presents the first three-dimensional FE model of UAT. It has been recently developed and the computational results, emerging from this 3D formulation, are discussed.

Model Description

General features

A detailed description of the our previously developed 2D numerical model can be found in [6, 12]. The current FE model utilizes the MSC MARC/MENTAT FE code [13] and is based on the updated langrangian analysis procedure that provides a transient analysis for an elastoplastic material and accounts for the frictional contact interaction between the cutter and workpiece as well as material separation in front of the cutting edge.

The relative movement of the workpiece and cutting tool in CT is simulated by the translation of the tool with the constant velocity. Harmonic oscillation with vibration amplitude of 15 μ m (peak-to-valley) is then superimposed on this movement in the tangential direction (i.e. along X-axis in Fig.1) in order to model ultrasonic vibration of the tool. The vibration speed is several times greater than the chosen translational speed of the tool leading to the periodic separation of the tool from the newly formed chip, thus transforming the process of cutting into one with a multiple-impact interaction between the tool and chip. Various stages of such vibration cycle are described in detail in [14].

The developed FE model is fully thermomechanically coupled in order to properly reflect interconnection between thermal and mechanical processes in the cutting zone: excessive plastic deformation and friction at the tool-chip interface lead to high temperatures generated in cutting region. This results in generation of thermal stresses and volumetric expansion as well as affects material properties of the workpiece, such as thermal conductivity and specific heat. More details on thermomechanical processes in UAT in comparison to CT can be found in [12].

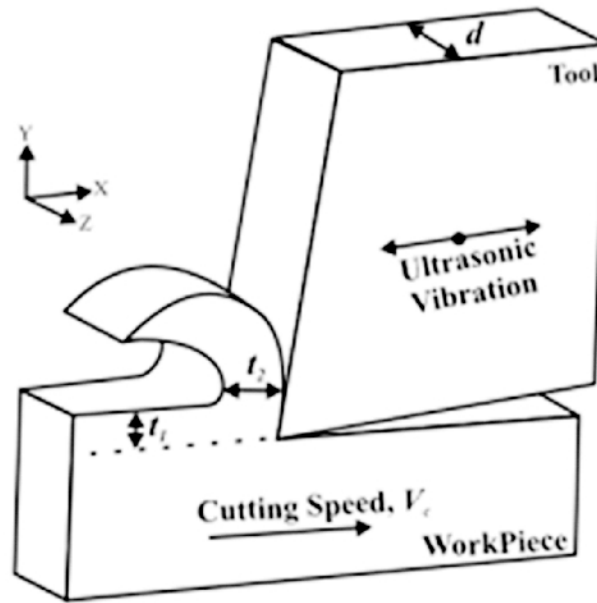


Figure 1: A scheme of the relative movement of the workpiece and cutting tool in 3D Simulations of UAT

The mechanical behavior of the work piece material (aged Inconel 718) at high strains, strain rates and elevated temperatures can be adequately described by the Johnson-Cook material model [15], accounting for the strain-rate sensitivity, that is employed in simulations (Fig. 2):

$$\sigma_y = (A + B \varepsilon_p^n) \{1 + C \ln[(d\varepsilon_p/dt)/d\varepsilon_0/dt]\} (1 - T^{*m}) \quad (1)$$

Where $A = 1241\text{MPa}$, $B = 622\text{MPa}$, $C = 0.0134$, $n = 0.6522$, $T^* = (T - T_{\text{room}})/(T_{\text{melt}} - T_{\text{room}})$, ε_p and $d\varepsilon_p/dt$ are plastic strain and a strain rate, T_{room} and T_{melt} are the room and melting temperatures, respectively. A term T^{*m} is assumed to be negligible since thermal softening of Inconel 718 is insignificant (less than 5%) within the temperature range that is modelled in FE simulations and justified by infrared thermography experiments. This material model, utilised by various researchers (see, e.g. [16, 17]), has been modified to prevent Unrealistically high stress values at high strains, so that maximum stress values are now limited to ultimate tensile strength of Inconel 718 at corresponding strain rates (that can reach 105 1/s for standard cases).

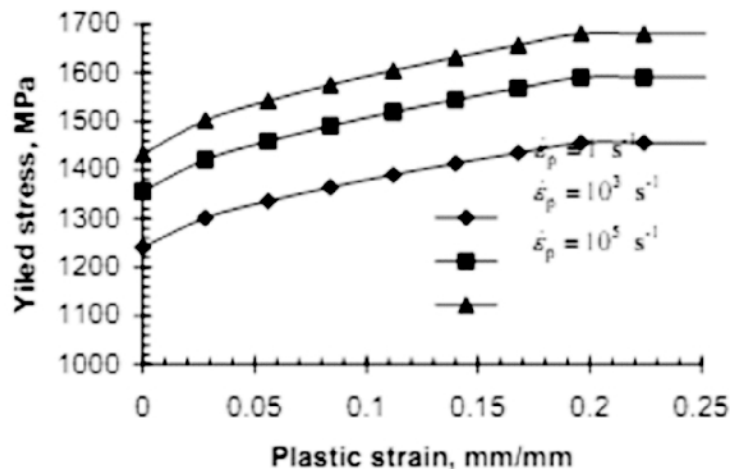


Figure 2: Effect of strain rate on plastic behaviour of Inconel 718

FE Model

A 3D model for orthogonal turning process, i.e. the one where the tool edge is normal to both cutting and feed direction, is considered. The dimensions of the part of the workpiece modeled in simulations are 2.5 mm in length by 0.5 mm in height by 0.4 mm in depth with the uncut chip thickness t_1 being 0.1 mm (Fig. 3). The material's properties adopted for the workpiece are those of Inconel 718. The cutting tool is simulated as a rigid body and the material properties defined are those of tungsten-carbide. The current model possesses a number of advantages compared to the 2D model. Various 3D effects in turning, such as non-orthogonal / oblique chip formation, as well as the influence of the tool geometry on process parameters (cutting forces and stresses generated in the workpiece material) could be studied.

The 3D model also permits to investigate the effect of various vibration directions of the cutting tip in UAT on the cutting process, and eventually should serve as an optimization tool for the UAT technology. Various combinations of vibration directions can also be studied numerically, whereas their experimental implementation can be extremely laborious, as it may require new types of ultrasonic transducers and mounting systems to be designed. Furthermore, the three-dimensional FE formulation helps to perform a direct comparison of numerical results and experimental tests for oblique cutting, thus not requiring any changes to a standard cutting setup. This is important since the FE results, e.g. cutting forces, based on the 2D model can be directly compared only to orthogonal turning tests. Such turning tests can be very difficult to implement for intractable materials, as they require special setup arrangements or specific workpiece shapes, e.g. thin tubes. In addition, the 3D model does not need as many assumptions as the 2D model, for example, the workpiece thickness is introduced here explicitly as compared to its artificial introduction in 2D. The 3D model also accounts for chip expansion in the lateral dimension (along Z-axis in Fig. 1) That was impossible in the 2D model and led to generation of excessive stresses in the cutting region.

Finally, the real geometry of the cutting tool can be studied with the 3D model, thus allowing the analysis of the influence of the tool sharpness and wear on the cutting process.

During the simulation, elements in the process zone can become highly distorted, and hence are no more appropriate for calculation. Automatic remeshing/rezoning is used in the workpiece and chip to replace those distorted elements with ones of better shape. Figure 4 shows the chip formed as a result of successful implementation of remeshing/reasoning.

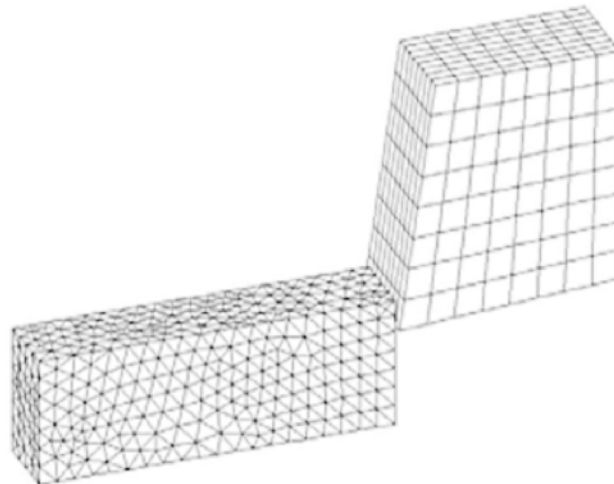


Figure 3: Finite-element mesh for the workpiece and cutting tool in the FE model

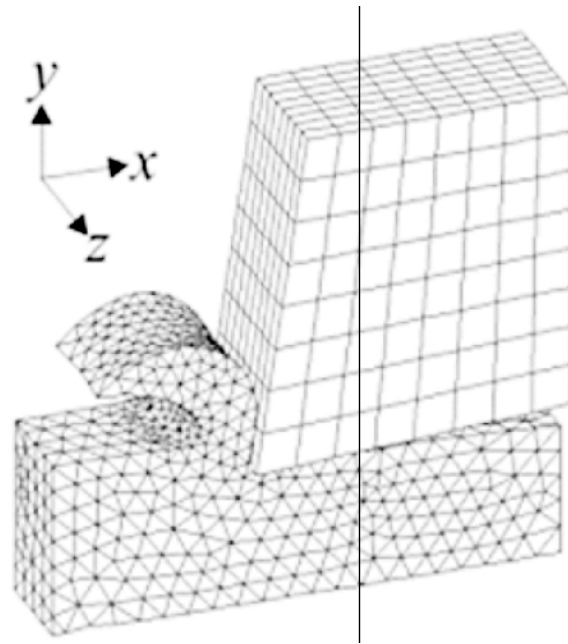


Figure 4: Chip formation in FE simulations

In nearly all models developed for the simulation of metal cutting, an initial cut was introduced in the work piece as the starting point for separation that leads to chip formation. The present FE model does not utilize such a cut (Figure 3). Hence, an adequate study of chip formation from its very beginning to a fully formed chip is possible. This type of modeling also provides the benefit of using the same model of the work piece for different shapes of the cutting tool thus forming a basis for optimization studies for the tool shape.

Results of Simulations and Discussion

All variants of numerical (finite element) simulations below are performed for two cutting techniques (CT and UAT) with identical parameters so that results for CT could serve as a reference for UAT. Two contact conditions are considered at the tool-chip interface: (a) a frictionless contact, and (b) a contact with friction (coefficient of friction $\mu = 0.5$). The former case corresponds to the well-lubricated cutting process, with heat generation occurring only due to plastic deformation processes. Case (b) models dry cutting conditions, with additional heat being generated due to friction between the tool surface and separated workpiece material.

Chip Shape Formation

Noticeable differences are observed between chip shapes obtained in FE simulations with and without friction for both CT and UAT. The radius of curvature of the chip under the frictionless contact condition at the tool-chip interface is approximately 2.5 smaller than that for the contact with friction of both CT and UAT (Fig. 3); that is supported by turning experiments with different lubricants, showing higher values of the radius of curvature for dry turning.

The chip thickness in simulations with friction is greater than that in simulations without friction. The chip thickness ratio $r = t_1/t_2$ (see Fig. 1), that is the ratio of thickness of the uncut chip to that of the deformed one, equals 0.6 and 0.7, respectively, for simulations with and without friction, for both CT and UAT. No significant differences between CT and UAT are found in the value of r for the same friction conditions. This numerical result is also in good agreement with experimental studies showing only insignificant variations in the chip thickness for both cutting schemes.

Cutting Forces

A significant difference in forces acting on the cutting tool has been discovered for UAT and CT for similar

cutting parameters. In CT simulations a practically non-changing force is acting on the cutting tool, while in UAT the forces start to increase with penetration and attain levels somewhat higher than the average force in CT at the maximum penetration depth. The force magnitude then starts to decline at the unloading stage until it vanishes when the cutter separates from the chip and starts to move away from it. The forces stay close to zero level until the cutter comes into contact with the chip again at the next cycle of ultrasonic vibration. The comparison of values from Fig. 6 shows that the averaged (over the vibration cycle) force in case of UAT is nearly 38% of the forces in case of CT. Low-level fluctuations of the cutting force at the withdrawal and approach stages of the cycles are explained by the remaining contact between the cutter and freshly formed work piece surface, as well as by the numerical error involved in FE simulations.

Effect of Lubrication/Friction

The significant difference in forces acting on the cutting tool has been discovered between simulations of UAT with and without friction (Fig. 5). The maximum magnitudes of cutting forces are reached when the tool is in full contact with the chip, with these forces dropping to zero levels when the tool disengages from the chip. The maximum magnitude of the cutting force in simulations with friction is by 20-25% higher than that in frictionless simulations.

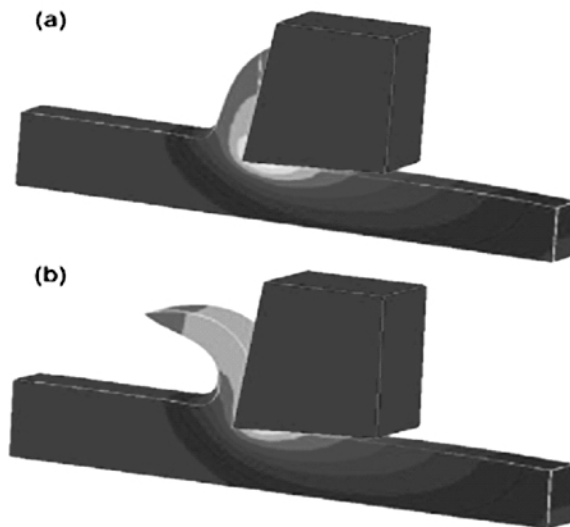


Figure 5: Chip shape and distribution of equivalent plastic strains in the cutting region in simulations of UAT with friction ($\mu = 0.5$) (a) and without it ($\mu = 0$) (b). Cutting parameters: $t_1=0.1$ mm, $V_c = 310$ mm/s ($t = 3$ ms)

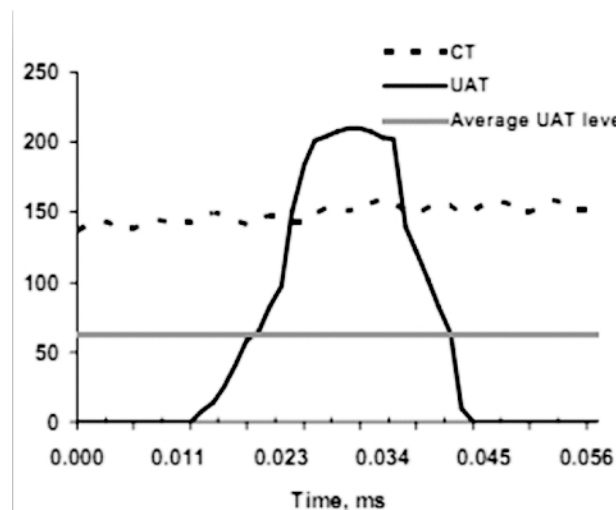


Figure 6: Comparison of calculated forces in cutting tool for CT and UAT simulations ($\mu = 0.5$, $t_1=0.1$ mm, $d = 0.4$ mm, $V_c = 335.2$ mm/s)

Ultrasonic Amplitude

FE simulations were conducted to study the effect of vibration amplitude on the forces acting on the cutting tool in UAT. An increase in the peak force with an increase in the amplitude was observed (Figure 8). However, the average cutting force decreases with an increase in the amplitude. A decrease of approx. 28% in the average force was recorded for an increase in.

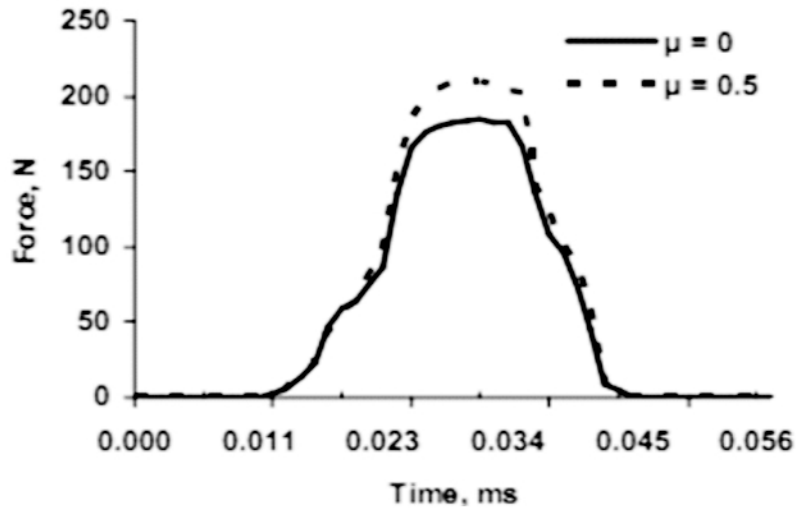


Figure 7: Comparison of calculated forces in the cutting tool for UAT with friction ($\mu = 0.5$) and without friction ($\mu = 0$) ($t_1=0.1$ mm, $d = 0.4$ mm, $V_c = 335.2$ mm/s)

Ultrasonic Frequency

A separate study was conducted to analyze the effect of ultrasonic frequency on the forces in the cutting tool (Figure). The results from these simulations show nearly the same peak force in the cutting tool in all three cases.

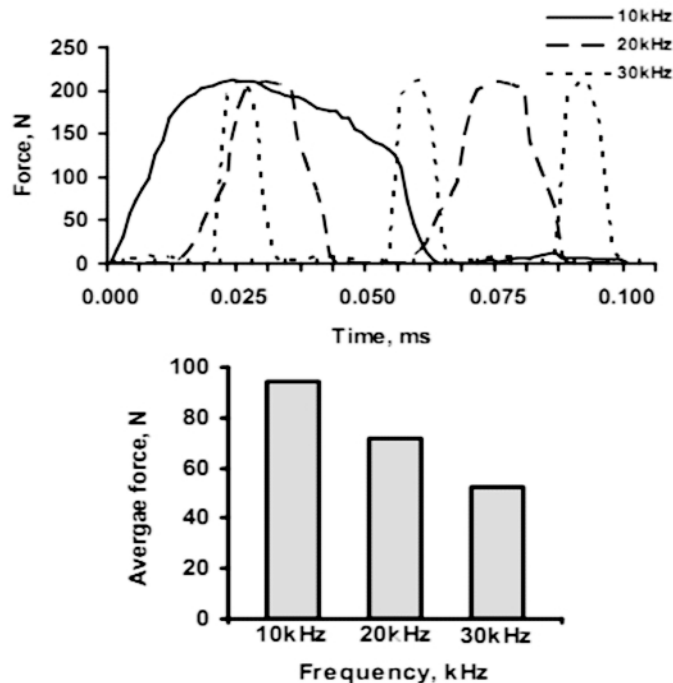


Figure 9: Effect of ultrasonic frequency on forces in cutting tool ($t_1=0.1$ mm, $d = 0.4$ mm, $V_c = 335.2$ mm/s)

The average force demonstrated a drop by approx. 24% for frequency increase from 10 kHz to 20 kHz and a further drop by approx. 26% when frequency was increased from 20 kHz to 30 kHz. It is important to mention that as the three cases have different frequencies so they all have unique time duration of their single vibration cycle. For the purpose of comparison of these cases, with each of them having a unique frequency, a common time scale was selected. Average of forces was then calculated over this time scale (0.1 ms) and comparisons were made.

Effect of Feed Rate

The effect of the feed rate on the stresses and forces in the cutting tool was studied for UAT. Two different feed rates - 0.1 mm and 0.2 mm - were used at a constant cutting speed of 80 rev/min. Zones of high stress intensity were observed with a higher level of feed rate, while the maximum value of the stress rate was the same for both cases (Figure 10). Figure 11 shows the effect of feed rate on the forces in the cutting tool; increasing the feed rate from 0.1 mm to 0.2 mm gave a 45% increase in the force level in the cutting tool.

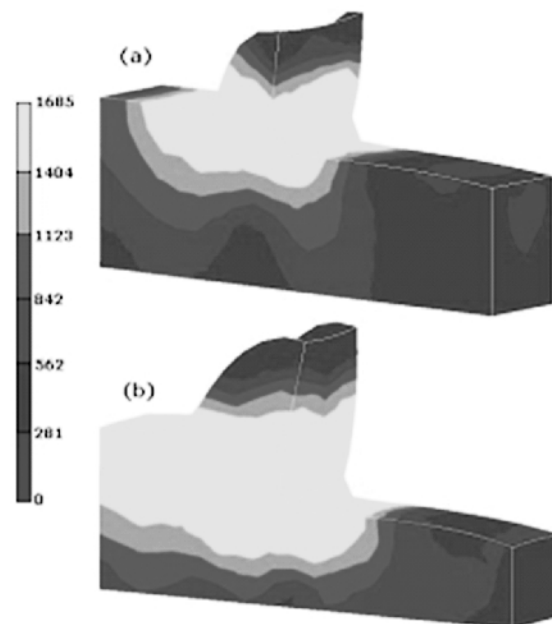


Figure 10: Stresses in the cutting region for various feed rates : 0.1 mm (a) and 0.2 mm (b) ($d = 0.4$ mm, $V_c = 335.2$ mm/s)

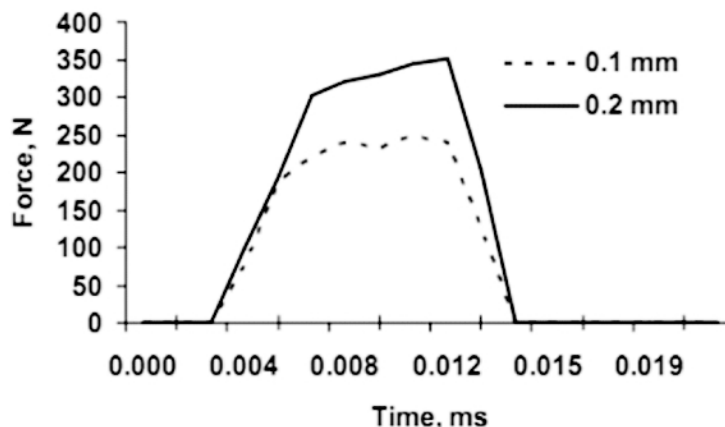


Figure 11: Evolution of forces in cutting tool during a cycle of vibration for feed rates 0.1 mm

Conclusion

A 3D thermo mechanically coupled FE approach was used to model UAT with CT forming a basis for comparative analysis. For the typical combination of vibration parameters ($f = 20$ kHz, $a = 15$ μ m) the calculated cutting force in UAT was 40% of that in CT, whilst the various feed rates [18]. The comparison of feed rates indicated a 45% increase in the level of cutting forces in simulations of UAT for doubling the feed rate from 0.1 mm to 0.2 mm due to a higher material removal rate in the latter case. Experimental results showed a 60% increase in the cutting force in UAT when the feed rate doubles from 0.05 mm/rev to 0.1 mm/rev [18], hence we can conclude a fair agreement between experimental and numerical results. The comparison of simulations with and without friction, corresponding to dry simulations led and lubricated turning conditions, respectively, showed that in the latter case the cutting force was 10-15% lower and in a good agreement with experimental results [18] indicating 30% decrease in the cutting force when the lubricant was applied. Simulations also showed that temperature along the cutting edge reach higher values in the middle due to the convective heat dissipation. An increase in the vibration amplitude from 7.5 μ m to 30 μ m in FE to a 52% decrease in the average cutting force in UAT and could be explained by an increased part of a cycle of ultrasonic vibration without a contact between the tool and chip. An increase in the vibration frequency from 10 kHz to 30 kHz resulted in a 47% drop in the level of average cutting forces, which could be attributed to an increased number of micro-impacts between the tool insert and the workpiece. Hence, an increase in either vibration frequency or amplitude leads to a decrease in cutting forces in the UAT process that is beneficial to increasing the accuracy of the cutting process and improving material removal rates.

References

- [1] Babitsky VI, Kalashnikov AN, Meadows A, Wijesundara AAHP: Ultrasonically assisted turning of aviation materials. *Journal of Materials Processing Technology* 2003, 132:157-167.
- [2] Babitsky VI, Kalashnikov AN, Molodtsov FV: Autoresonant control of ultrasonically assisted cutting. *Mechatronics* 2004, 14:91-114.
- [3] Stashev VK, Babitsky VI: Ultrasonic cutting as a nonlinear (vibro-impact) process. *Ultrasonics* 1998, 36:89-96.
- [4] Trent EM, Wright PK: *Metal Cutting*: Butterworth-Heinemann, London; 2000.
- [5] Childs THC, Maekawa K, Obikawa T, Yamane Y: *Metal Machining: Theory and application*: Arnold Publishers; 2000.
- [6] Mitrofanov AV, Babitsky VI, Silberschmidt VV: Finite element analysis of ultrasonically assisted turning of Inconel718. *Journal of Materials Processing Technology* 2004, 153-154:233-239.
- [7] Anagonye AU, Stephenson DA: Modeling cutting temperatures for turning inserts with various tool geometries and materials. *Journal of Manufacturing Science and Engineering (Trans ASME)* 2002, 124(3):544-552.
- [8] Pantale O, Bacaria JL, Dalverny O, Rakotomalala R, Caperaa S: 2D and 3D numerical models of metal cutting with damage effects. *Computational Methods for Applied Mechanical Engineering* 2004, 193:4383-4399.
- [9] Ceretti E, Lucchi M, Altan T: FEM simulation of orthogonal cutting: serrated chip formation. *Journal of Materials Processing Technology* 1999, 95:17-26.
- [10] Ramesh MV, Seetharamu KN, Ganesan N, Kuppuswamy G: Finite element modeling of heat transfer analysis in machining of isotropic materials. *International Journal of Heat and Mass transfer* 1999, 42:1569-1583.
- [11] Strenkowski JS, Shih AJ, Lin JC: An analytical finite element model for predicting three-dimensional tool forces and chip flow. *International Journal of Machine Tools & Manufacture* 2002, 42:723-731.
- [12] Mitrofanov AV, Babitsky VI, Silberschmidt VV: Thermomechanical finite element simulations of ultrasonically assisted turning. *Computational Materials Science* 2004, 32:463-471.

- [13] Borst R: Numerical aspects of cohesive-zone models. *Eng Fract Mech* 2003, 70:1743-1757.
- [14] Babitsky VI, Mitrofanov AV, Silberschmidt V V: Ultrasonically assisted turning of aviation materials: simulations and experimental study. *Ultrasonics* 2004, 42:81-86.
- [15] Johnson G, Cook W: Fracture characteristics of three metals subjected to various strains, strain rates, temperatures and pressures. *Engineering Fracture Mechanics* 1985, 2(1):31-48.
- [16] Ng EG, El-Wardany TI, Dumitrescu M, Elbestawi MA: Physics-based simulation of high speed machining. *Machining Science and Technology* 2002, 6(3):301-329.
- [17] Maudlin P, Stout M: Metal cutting simulation of 4340 steel using an accurate mechanical description of material strength and fracture. *Minerals, Metals and Materials Society* 1996:29-41.
- [18] Mitrofanov AV: Modelling the ultrasonically assisted turning of high-strength alloys. Doctoral Thesis. Loughborough: Loughborough University; 2004.

An Analytical Finite Element Model for Tool-Chip Contact Area for Orthogonal Cutting

Muhammad Shoab¹

Abstract

In this paper the origin of chip forms and how one could develop analytical and computational models of the mechanics is tried to understand. Geometry is often the key to solve chip deformation under different loadings. Irrespective of whether a chip is free or obstructed, the initial geometry of the chip is decided by the kinematics conditions prevailing at the moment the chip first leaves the tool-chip separation line (TCSL). The chip at the TCSL may be called the origin chip (OC). If the tool rake face is plane, the TCSL can be expanded to be a straight segment. It is noted that the generalized trajectory of a particular leaving the TCSL is a 3-D helix that is completely expressible. The deformed chip is totally different in form from the initial chip. If so, what would be the geometric properties that would be preserved during the additional deformation of the chip? What are the internal geometric constraints leading to these invariants? The aim is to explore these apparently theoretical questions in the belief that the identification of such geometric invariants and constraints, if any would be of practical value in the analysis of the mechanics of chip and eventually, in obtaining a fundamental of the conditions that best promote chip formation. In general, in physical sense, the entity we call a chip is born at the primary plastic deformation zone that emanates from the cutting edge and spreads towards the junction between the work and chip surfaces. The form of this chip is a result of the total deformation the work material had experienced at the zone. However the primary chip usually, experiences 'environmental' influences owing to its interaction with the tool as it traverses the chip-tool contact zone.

Keywords: Finite Element Model, Tool-Chip, Orthogonal Cutting, Cutting Process

Introduction

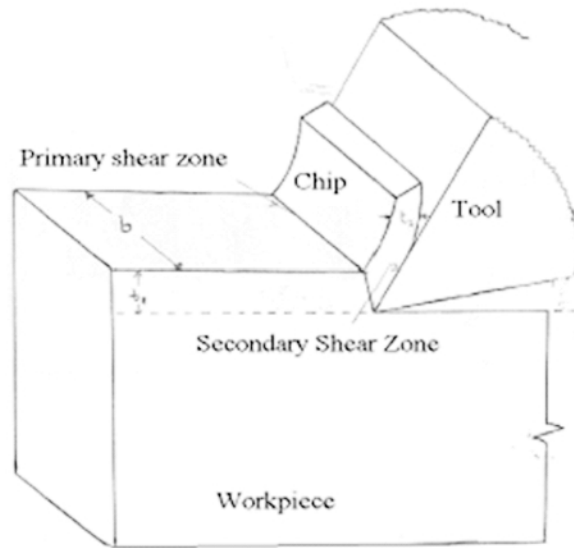
Metal cutting involves concentrated shear along a rather distinct shear plane. As metal approaches the shear plane, it does not deform until the shear plane is reached. It then undergoes a substantial amount of simple shear as it crosses a thin primary shear zone. There is essentially no further plastic flow as the chip proceeds up the face of the tool. The small amount of secondary shear along the tool face is generally ignored in a first treatment of the cutting process, and the motion of the chip along the tool face is considered to be similar to that of friction slider of constant coefficient.

The back of a chip is rough due to the strain being inhomogeneous. This is due to the presence of points of weakness or stress concentration present in the metal being cut. A shear plane passing through a point of stress concentration will deform at a lower value of stress than one that does not include a point of stress concentration. The cutting tool moves through the work material producing a finished surface on the work piece and the chip, which is removed from the work material. The deformation process, which takes place in metal cutting, is unique in many respects. The large-scale plastic deformation which takes place occurs in a small, relatively unconstrained volume called the shear zone. To adequately study the mechanics of the metal cutting process, the boundary conditions on the entire shear zone must be taken into account. Additionally, the present investigation of the mechanics of the metal cutting process differs from most

Previous work in this area in that no a priori assumption about the nature of the zone of deformation is made. In the present work the analysis is one of a material subjected to a known displacement, the boundary conditions imposed being such that the metal cutting process is approximated. The tool moves through the work piece with velocity, V , removing part of it, the chip, and producing a finished surface. The tool can be described by its rake angle " α " and the material being removed is defined by the depth of cut " t " and the width of cut " b ". The easily described situation where the tool moves parallel with the work surface while the tool edge is perpendicular to the cutting velocity is called orthogonal cutting. The depth and width of cut are constant.

¹Industrial & Manufacturing Engineering Department NED, University of Engineering & Technology, Karachi.

At low cutting speeds or when cutting a material containing points of stress concentration discontinuities chips may form.



Secondary Shear Zone

The secondary layer is a portion of the chip that has been rendered unusually plastic as a result of high temperatures. The temperature in this layer will definitely be above the strain recrystallization point and even lie above the $\alpha \rightarrow \gamma$ phase — transformation temperature, in the case of steels. Temperatures in the layer will be sufficiently high to enable carbon tungsten from the tool material do diffuse into the chip. (Carbon will diffuse particularly rapidly if the zone has transformed to γ -iron). If the secondary shear zone is moving relative to the tool face, wear is apt to be rapid since the carbon will be rapidly convected away by the chip. It is highly advisable that the secondary shear zone become affixed to the tool face in order to avoid the rapid removal of diffused material. Titanium carbide appears to help from a thin stationary secondary shear zone on the tools. At the same time TiC lowers the thermal conductivity of the tool and hence the speed at which the protective (stationary) secondary shear zone will form.

Previous Work

The first quantitative work was that of Zovrykin who in 1983, studied the planting operation. Assuming a shear plane and the force along it to be a minimum, he arrived at an expression for the angle between the shear plane and the finished work surface, the so-called shear angle φ . The Result is

$$\varphi = 450 + \alpha/2 - \beta/2 - \beta'/2 \quad (1)$$

Where α is the tool rake angle, β is the friction angle between the chip and the tool, and β' is a friction angle for the shear plane. In 1986 Hermann arrived at an expression for the shear angle based on the assumption that the shear plane is that of maximum stress. The result of this analysis is

$$\varphi = 450 + \alpha/2 - \beta/2 \quad (2)$$

Thermo-mechanical Explanations

This explanation is that large-scale plastic deformation will occur in localized regions when the temperature in this region exceeds a critical value. The analysis is built on the assumption of a plane source of heat

generation in an adiabatic work material as it passes through the shear zone resulting in thermal weakening of the work material when the effect of strain hardening is overcome by thermal effects. Neglecting strain-rate effects and assuming constant values for thermal conductivity (k), specific heat (c), and density (ρ), and no increase in internal energy of the chip or work, the one-dimension heat condition equation becomes

$$C \rho \frac{\partial T}{\partial t} - K \frac{\partial^2 T}{\partial x^2} = \tau \dot{\gamma} \quad (3)$$

τ and $\dot{\gamma}$ being the shear stress and shear strain rate respectively.

Mechanistic Explanations

The varying shear angle will cause varying chip thickness, and for cyclic variations of the shear angle, a chip, which exhibits an apparently lamellar structure, can result. Landberg to changing frictional characteristics of the process as work material passes through the shear zone and along the tool face and Eugene to a variation of the rate of propagation of plastic deformation with depth below the surface of the work piece. There is also what may be considered a third general explanation of a unstable deformation in metal cutting. Similar to the thermal instability theory, a negative slope in the work material's stress-strain behavior is proposed, not due to thermal strain softening, but rather to the formation of voids in the work material as it passes through the shear zone. Interior regions the shear zone makes no mention of any void formation.

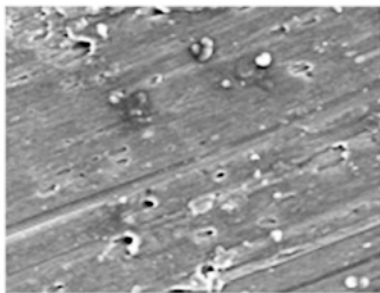


Figure 1

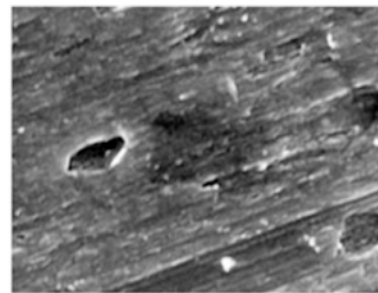


Figure 2

Figure 1. The top and side of an aluminum chip produced by orthogonal cutting at a depth of 0.0035 in. and a width of 0.050 in. Using a 25 rake angle tool is shown here. Again the characteristics lamellar structure is in evidence, however, the well-defined structure is not maintained from the top around and down the side of the chip but its connection with the structure on the chip top is not clear. No sharp boundary exists between the top and side of the chip but a gradual transition around this expected corner is seen.

Figure 2 the top and sides of an aluminum chip are shown. This chip was produced by shoulder cutting with $t = 0.008$ in., $b = 0.127$ in., and $\alpha = 30^\circ$. fig. 2 is an electron micrograph of the top and outside or initially free side of the chip (100x) and shows the top and the inside or initially- constrained side of the chip (120x). visualized, where as a rounding of the top-side junction seems to have taken place on the constrained side of the shoulder cut.

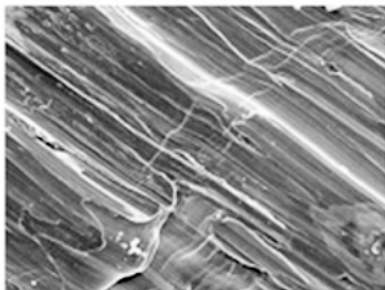


Figure 3

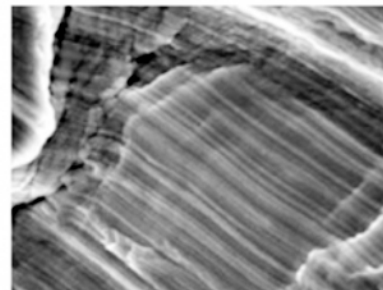


Figure 4

Figure 3 again shows the top and sides of an aluminum chip. In this case, however, the chip was produced in a groove cutting operation, $b = 0.129$ in. $\alpha = 400$. Fig. 7 shows, at 200x, a chip produced at a depth of cut of 0.005 in. and 8 is a 300x view of a chip whose undeformed thickness, t , was 0.002 in.

Figure 4 These are top views of an orthogonally-produced copper chip. The width and depth of cut were, respectively, 0.050 in. and 0.020 in. The tool rake angle was 250. Fig. 4 is a 75x view of the initial region of the chip, that is, the start of cutting .the cutting direction being from the top of the figure downward. The characteristic chip structure is not developed until some distance from this initial end of chip.

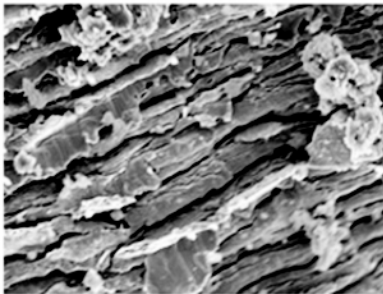


Figure 5

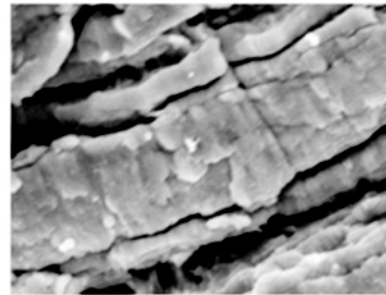


Figure 6

Figure 5 Shown are the top and side of the initial region of a brass chip at 50x. This chip was produced using a 250 rake angle tool cutting at the depth of 0.040 in. The width of the cut was 0.050 in. Again, the only structure seen on the chip is parallel to the cutting direction. A lateral flow of the work material can be seen near the top-side edge of this chip, and lateral flow is indicated over the entire side of the chip. The side surface of the work piece was initially smooth and its appearance was similar to that of the top of the work piece seen here.

Figure 6 Optical micrographs (27x) show longitudinal sections of the initial end of brass chips produced in orthogonal cutting with $b = 0.050$ in. and $\alpha = 25$. These specimens are longitudinal sections of chips produced by cutting the initial region of the chip at the mid-plane of the width of cut. The cutting direction in this figure is from right to left.

This series of chip sections indicates an initial period of deformation before chip production with constant microscopic chip thickness is achieved. The length of the region of increasing chip thickness is greater than, but of the same order as, the thickness of the chip in the constant thickness region. When t/b is very small ($t/b < 0.04$), the cross sections of the chips produced are approximately rectangular. As t/b increases, two processes modify the chip cross section shape. The top surface of the chip becomes curved and the initially vertical sides of the chip become inclined to the vertical. These two processes occur at differing rates and start to occur at different values of t/b , depending on the work material.

Finite Element Analysis

Outline of Finite Element Analysis

The relatively large amount of lateral material flow near the free sides of the shear zone can be seen clearly in the micrographs of chip cross sections .The desirability of a true three dimensional solution is obvious. The state of three-dimensional flow can be described by the equations of equilibrium, the flow rule, and the yield condition which follow in this order.

$$\frac{\partial \sigma_{ij}}{\partial \sigma_i} = 0 \quad (4)$$

$$d\epsilon_{ij}^p = \frac{d\lambda}{\partial \sigma_{ij}} \frac{\partial F}{\partial \sigma_{ij}} \quad (5)$$

$$S_{ij} S_{ij} = 2/3 \sigma_y^2 \quad (6)$$

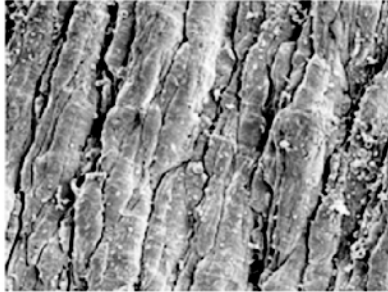


Figure 7

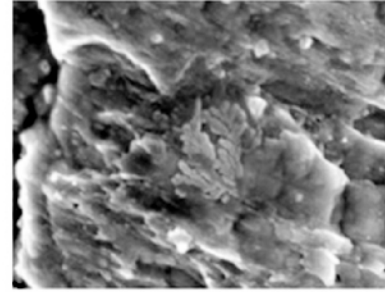


Figure 8

In these equations, σ_{ij} are stresses, X_j are the coordinate system directions, $d\epsilon_{ijp}$ are the plastic increments, and S_{ij} are the stress deviations, i.e.,

$$S_{ij} = \sigma_{ij} - 1/3 \sigma_{kk} \delta_{ij} \quad (7)$$

is a constant, σ_y is the yield strength of the material, and F is a functional representation of the yield surface. This system of equations is not amenable to easy solution. In the finite element methods of analysis the structure is assumed to be composed of a number of discrete elements. The deformation of the structure is described by the displacements of nodes on the individual elements, which make up the structure. The deformation in the elements is defined in terms of the elements' nodal displacements by suitable shape functions, which make deformation and strain in contiguous elements compatible. The nodal displacement in the structure for a given applied load is obtained by solving for the displacement which will minimize energy functional describing the system. For example, using the Rayleigh-Ritz method of analysis, the unknown equilibrium deformation u is approximated by a sum of n known shapes N which satisfy the kinematics boundary conditions.

$$u_n = \sum_{i=1}^n a_i N_i$$

The evaluation of the numerical coefficients a_i is carried out so that they optimize the solution. One possibility is to determine the a_i on the basis that they will minimize the total potential energy of the system at its equilibrium configuration. The strain energy U and potential energy of the loading system V can be evaluated in terms of u_n and then a_i determined from the n equations,

$$\frac{\partial}{\partial a_i} [U(u_n) + V(u_n)] = 0 \quad (8)$$

In the finite element displacement method, which is used here the nodal displacements are unknowns. B. Finite Element Modeling

In the finite element method of analysis the structure of interest is, assumed to be composed of discrete elements which are connected at only a finite number of points. The points of connection are called nodes and the forces, which act at the nodes, are assumed to be representative of the distributed loading in the actual structure. For an element subjected to loads, P , the load deformation relation is $P_i = K_{ij} u_j$ being the load at node m in the i direction. K_{ij} is called the element stiffness matrix and the u_j are nodal displacements. Repeated indices imply summation. The problem now becomes one of determining the load-displacement characteristics of the elements, i.e., a determination of K_{ij} . The following discussion outlines this procedure.

$$P_i^m = K_{ij}^{mn} u_j^n \quad (9)$$

The displacement field in an element in terms of the nodal displacements is defined by the relationship

$$u_i = N^m u_i^m \quad (10)$$

Where u_i is the displacement in the i direction, u_{im} is the displacement at node m in the i direction, and N^m is the shape function corresponding to node m . Shape functions are discussed in the following. With displacements throughout the element known, the strains in the element can be determined from substituting the values of u from equation (10) the strains in the element are given in terms of the nodal displacements and derivatives of the shape functions as

$$\epsilon_{ij} = B_{ijk}^m u_k^m \quad (11)$$

B is an array of shape function derivatives which relates strain to nodal displacements. The relation between elastic stresses and strains is

$$\sigma_{ij}^e = D_{ijkl} \epsilon_{kl} \quad (12)$$

Where D is the elasticity matrix. Upon substitution of equation (12) in to (13) and using principle of virtual displacements for a set of nodal forces, P_i , the load-displacements relation, is obtained as

$$P_i^m = [\int_{vol} (B^T D B) d vol] u_j^n$$

Comparing this result to equation (9) gives an expression for the element stiffness matrix

$$K = \int (B^T D B) dV \quad (13)$$

For the 20-node element used (see following section) suitable shape functions in terms of local coordinates are Corner nodes:

$$N_i = 1/8 (1 + q_0) (1 + r_0) (1 + s_0) (q_0 + r_0 + s_0 - 2)$$

Midside nodes :

$$N_i = 1/4 (1 - q^2) (1 + r_0) (1 + s_0) \quad q_i = 0$$

$$N_i = 1/4 (1 - r^2) (1 + q_0) (1 + s_0) \quad r_i = 0$$

$$N_i = 1/4 (1 - s^2) (1 + q_0) (1 + r_0) \quad s_i = 0$$

In which $q, r,$ and s are the local element coordinates, $q_0 = q_{q_i}, r_0 = r_{r_i}, s_0 = s_{s_i}$

And the i indicates the local node number.

The strain displacement relationships given by equation (11) and (12) are in terms of the global (x, y, z) derivatives of the shape functions. The transformation of the local coordinate system derivatives to the Global system is carried out using the Jacobian matrix.

As the stiffness matrix for each element is formed the boundary conditions are applied. A zero displacement for a node is incorporated by zeroing the row and column in the stiffness matrix and the load term corresponding to the fixed displacement and defining the diagonal term as unity.

$$K_{ij}^{mn} u_j^n = P_i^n$$

References

- [1] Merchant, M. E, "Mechanics of the cutting process," J. Appl. Phys., Vol. 16, 1945, pp. 267 and 318.
- [2] Shaw, M.C.Cook, N. H. and Finnie, I. , "The Shear Angle Relationship in Metal Cutting, "Trans. ASME, Vol. 75, 1953, p.273.
- [3] Sata, T. and Yoshikawa, H. "Recent Developments Concerning Cutting Mechanics, "Proc. Conf. Intl. Res. Prod. Eng. ASME 1956.

Analysis of Thickness Effect on Piezoelectric Beam

Riffat Asim Pasha¹, Zahid Suleman² and M. Z. Khan³

Abstract

There is increasing demand for developing smart structures in various electronic and electromechanical systems during past two decades. More recent innovations like Micro-Electromechanical system (MEMS), Nano structures, Electronic chips, and Printed Circuit Boards etc, have remarkable role in the field of electronics. The modeling analyzing and manufacturing of these small-scale components remained always a challenging job. Finite element capability available in commercial software package ANSYS makes it convenient to perform modeling and analyzing of these smart structures. A piezoelectric cantilever beam analyzed for different thicknesses. Voltage change in each electrode along with other related properties/parameters were found. Thickness variation produced remarkable important results which can be used for optimizing the thickness range in these smart materials. Voltage percentage per electrode determined and different nodal solutions were obtained. Various recommendations have been suggested to analyze such smart material before using in various applications for the generation and actuation systems and for their reliability and durability.

Keywords: Piezoelectric Beam, Finite Element Modeling, ANSYS

Introduction

Recently the piezoelectric materials are extensively used in electromechanical and micro electromechanical actuators and sensors. Finite Element Analysis is extensively used for the modeling of such materials. "ANSYS" is useful to simulate the structure of piezoelectric devices successfully and accurately. Electromechanical coupled-field finite element modeling (FEM) accurately predict the resonant frequency and harmonic response of the system subjected to a step voltage input [1].

The researchers describe the FEM capabilities in modeling and analyzing of various electronic parts. An accurate numerical modeling of the stress and strain fields in electronic packages is Imperative for the improvement of current and future mechanical design of electronic packages [2].

The development of Finite Element codes incorporating smart material element has provided an opportunity to solve some practical problems [3]. The solder joint lifetime for two different models was earlier analyzed by ANSYS and it was concluded that the solder joints closer to the die edge (away from die center) are more susceptible to elasto-plastic fatigue damage [4].

Finite Element Modeling

The basic equations for the electromechanical finite element analysis are,

$$\begin{aligned} T &= [c] (S) - [e] (E) \\ D &= [e]^T (S) + [\epsilon] (E) \end{aligned}$$

The above equations are the structural and electrical constitutive equations respectively. The matrices c , e , and ϵ contains the materials property data of the piezoceramics, where as the piezoelectric materials are described by compliance matrix, "S", piezoelectric strain matrix, "d", and the dielectric matrix, "ε" [5]. Piezoelectrics is the coupling of structural and electric fields, which is a natural property of materials such as quartz and ceramics. Applying a voltage to a piezoelectric material creates a displacement, and vibration of piezoelectric material generates a voltage. A typical application of piezoelectric analysis is a pressure transducer, possible piezoelectric analysis types are static, modal, harmonic, prestressed, and transient [6]. Many experimental and theoretical studies of the frequency spectra of resonant vibration in disks of isotropic and piezoceramic materials with varying diameter/ thickness ratio have been reported [7,8,9,10].

^{1,2&3} Department of Mechanical Engineering, University of Engineering & Technology, Taxila.

Piezoelectric disks with a front layer of varying thickness have been investigated using the FE method [11]. Some investigations of piezoceramics disks using the Finite Element Method have been reported [12,13].

Piezoelectric Beam Description

A piezoelectric 2-D cantilever beam of length L, having electrodes mounted on the upper surface was modeled. The properties of the PVDF material are described in Table-1.

Table 1: Properties of PVDF

Young's Modulus, E_1 (N/m ²)	Poisson's Ratio, ν_{12}	Shear Modulus, G_{12} (N/m ²)	d_{31} (C/N)	d_{32} (C/N)	d_{33} (C/N)	$(\epsilon_{33})^{-1}$
2.0E9	0.29	0.775E9	2.2E-11	0.3E-11	-3.0E-11	12

Table 2: ANSYS analysis results

Thickness (mm)	1E-05	5E-05	6E-05	7E-05	8E-05	9E-05	3E-04	5E-04	1E-03	1.5E-03
Electrode1	11.93	2.986	4.299	5.853	7.639	9.666	107.127	295.213	1167.076	2603.66
Electrode2	10.691	2.673	3.852	5.237	6.843	8.671	95.873	266.713	1062.686	2410.592
Electrode3	9.427	2.357	3.391	4.62	6.033	7.627	84.831	235.358	939.393	2082.573
Electrode4	8.164	2.041	2.939	4	5.225	6.613	73.454	203.837	813.827	1826.193
Electrode5	6.903	1.726	2.485	3.382	4.418	5.592	62.096	172.354	688.153	1545.403
Electrode6	5.644	1.411	2.032	2.77	3.612	4.573	51.091	140.923	562.655	1268.296
Electrode7	4.387	1.097	1.582	2.146	2.808	3.564	39.184	109.543	437.383	1006.925
Electrode8	3.132	0.783	1.126	1.536	2.005	2.528	28.215	78.218	312.53	683.957
Electrode9	1.879	0.469	0.676	0.921	1.202	1.522	16.946	47.09	189.751	432.269
Electrode10	0.648	0.159	0.23	0.314	0.412	0.523	6.198	18.23	82.152	207.215
Total Voltage	62.805	15.702	22.612	30.779	40.197	50.879	565.015	1567.479	6255.606	14067.08
%age increase in thickness	0.00	80	83.333	85.714	87.5	88.888	96.666	98	99	99.333
%age increase in total voltage	0.00	-299.9	177.75	104.051	-56.243	23.439	88.884	95.993	98.996	99.553

A linear static analysis was performed for variable thicknesses. The electrode voltage for the actuation mode was taken as 100 Volt and the tip displacement for the sensors mode was 10mm. PLANE223, coupled-field 8-noded quadrilateral element type was selected which needs not to define any real constant.

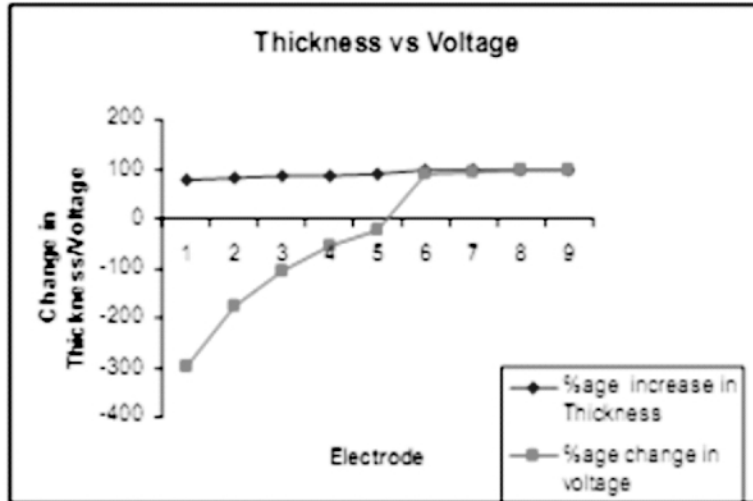


Figure 1: Thickness versus Voltage

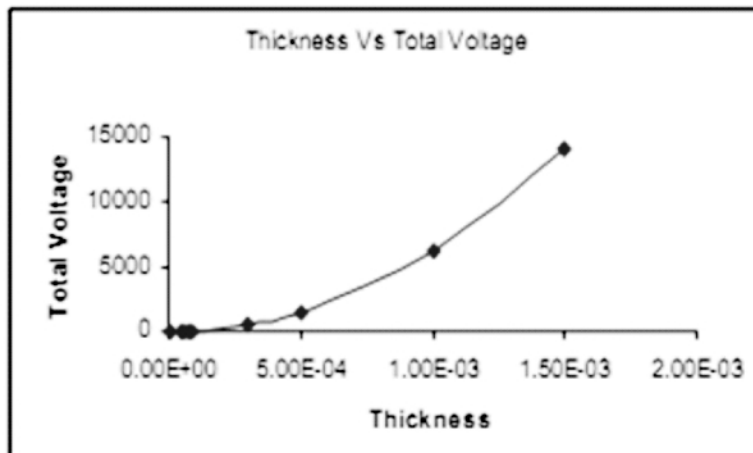


Figure 2: Thickness versus Total Voltage

Results and Discussions

Table-2 contains the results taken by analyzing various thicknesses and their effect on Electrode1 to electrode10 by using ANSYS package.

Nine different thicknesses were chosen and by Applying the displacement at the end of the beam there corresponding voltages were obtained. Figure1 indicates the %age thickness corresponding to the electrodes. It shows that initially the difference between the two parameters is large and gradually this difference gets closer and closer. At electrode no 6 the two values approximately overlapped. This phenomenon forwarded up to the last electrode and the minimum difference obtained at this value of %age increase in thickness.

Figure 2 indicates the behavior of increase in total voltage with respect to increase in thickness. It is observed that behavior remained constant i.e. total voltage was proportional to its corresponding increase in thickness except for first two initial thickness values where this behavior was reversed.

Conclusion

Piezoelectric cantilever beam was analyzed for various thicknesses and total voltage across the electrodes was found out. Percentage increase in thickness and corresponding total percentage increase in voltage

with respect to first electrode was determined. It is concluded that by gradually increasing the thickness values, the difference between the percentage increase in total voltage and percentage increase in thickness which was initially large becomes closer and closer and an optimal thickness value obtained where the total voltage attains a maximum value. Sensitivity of these smart structures can be analyzed by considering the closer values to get the maximum output. The optimal designing through modeling is recommended by obtaining various nodal solutions of different geometries to have reliability and durability of the final product.

Nomenclatures

E_1	= Young's Modulus
ν_{12}	= Poisson's ratio
G^{12}	= Shear Modulus
d_{31}, d_{32}, d_{33}	= Piezoelectric strain coefficients
$(\epsilon_{33})^T$	= Relative permittivity at constant stress
D	= Electric flux density vector
E	= Electric field vector
S	= Strain vector
T	= Stress vector
C	= Elasticity matrix
e	= Dielectric matrix

References

- [1] Wu, D. H., Chien, W. T., Yang, C. J., Yen, Y. 2005, Decoupled field analysis of piezoelectric beam actuator using FEM. *Sensors and Actuators A* 118(2005) 171-176
- [2] Erdogan Madenci, Ibrahim Guven, Bahattin Kilic, , 2003 *Fatigue life prediction of solder joints in electronic packages with ANSYS*, Kluwer Academic Publishers.
- [3] Riffat Asim Pasha, M.Zubair Khan, December, 2006 Lahore "Recent Developments In Piezoelectric Ceramics Materials and Deteriorations of their Properties" 2nd International Conference On Frontiers Of Advanced Engineering Materials (FAEM-2006) 04-06 .
- [4] Riffat Asim Pasha, H. Sana Ullah, M. Z. Khan, "Estimate the Thermomechanical Fatigue Life of Two Flip Chip Packages, 9th International Symposium On Advance Materials (ISAM-2005), 05-205
- [5] *Sensors magazine Online-1998- Using Coupled -Field Finite Elements to Characterize Piezoceramic Materials.*
- [6] ANSYS Release 10.0, Documentation.
- [7] E.A.G.Shaw, 1956 "On the resonant vibrations of thick Barium Titanate disks", *J. Acoust. Soc. Acoust. Soc.Am.* vol.28, pp. 38-50.

- [8] S. Ikegami, L. Ueda, and S.Kobayashi, 1974 "Frequency spectra of resonant vibration in disk plates of PbTiO₃ piezoelectric ceramics", J. Acoust. Soc. Am., vol.55, pp. 339-344.
- [9] S. Ueha, S. Sakuma, and E.Mori, " Measurement of vibration velocity distributions and mode analysis in thick disks of Pb (ZrTi) O₃", J. Acoust. Soc. Am. 1983 vol.73, pp. 1842-1847.
- [10] D. C. Gazis and R. D. Mindlin, 1960 "Extensional vibrations and waves in a circular disk and a semi-infinite plate," J. Appl. Mech., vol. 27, pp. 541-547.
- [11] Jan Kocbach, Per Lunde and Magne Vestrheim, , 1999 "FE Simulations of Piezoceramic Disks with a Front Layer of Varying Thickness", Proceedings of IEEE International Ultrasonics Symposium.
- [12] H. A. Kunkel, S. Locke, and B. Pikeroen, 1990 , "Finite-element analysis of vibrational modes in piezoelectric ceramic disks,"IEEE Trans. Ultrason. Ferr. Freq. Contr.", vol. 37, pp. 316-328.
- [13] N. Guo and P. Cawley, 1992 " Measurement and prediction of the frequency spectrum of piezoelectric disks by modal analysis", J. Acoust. Soc. Am., vol. 6, pp. 3379-3387.

Guidelines And Information For Authors

General

Papers may be submitted any time throughout the year. After having received a paper it is sent to three referees, at least one from a technology advanced countries. Papers reviewed and declared fit for publication before 31 December are published next year before 31 March every year. Papers must be submitted on a CD with FOUR Hard copies to the editor Technical journal, University of Engineering and Technology Taxila. Soft copy by e-mail to the following address is preferred.

technical.journal@uettaxila.edu.pk

Authors are required to read the following carefully for writing a paper.

Text

Text should be type-written with M.S word, Arial Font size 10.at single space and with margins as 1.5 inch top, 1 inch right, 1 inch left and 1 inch bottom, on an A-4 size, paper. The title page should include; the title; the name/names of the authors and their addresses, an abstract of about 200 words and keywords followed by the introduction. The text of the paper may be divided into introduction, methodology/Analysis results and discussion, conclusion, references and acknowledgment (if any). All pages should consist of single columns text.

Length

Research paper should not exceed 15 pages as per specifications given above.

Elements of Paper

The basic elements of paper are listed below in the order in which they appear: Title, names of the author and affiliations, Abstract, Body of paper, Acknowledgments, Nomenclature, references, Appendices.

Title

The title of the paper should be concise and definitive.

Names of Authors and Affiliations

Names of authors should consist of first name (or initial), middle initial and last name. The author affiliation should consist of his full address.

Abstract

An abstract up to a maximum of 200 words should open the paper. The abstract should give a clear indication of the objectives, scope and results, the abstract text may be organized to include the background, methods, results and conclusions.

Keywords

Keywords should be included on a separate line at the end of the abstract.

Body of the Paper

Body of the paper may include introduction and literature review, materials and methods, modeling/experimentation, results-discussions and conclusions.

Originality

Only original contributions to engineering and Science literature should be submitted for publication. It should incorporate substantial information not previously published.

Accuracy

All the technical, scientific and mathematical information contained in the paper should be checked with great care.

Use of SI Units

Preferably SI units of Measurements be included.

Mathematics

Equations should be numbered consecutively beginning with (1) to the end of the paper. The number should be enclosed in parentheses (as shown above) and set flush right in the column on the same line as the equation. This number then should be used for referring the equation within the text. Equation may be referenced within the text as "Eq. (x)". When the reference to an equation begins a sentence, it should be spelled out fully, as "Equation (x).in all mathematical expressions and analyses, symbols (and the units in which they are measured) not previously defined in nomenclature should be explained.

Figures

All figures (graphs, line drawings, photographs, etc.) should be numbered consecutively and have a caption consisting of the figure number and a brief title or description of the figure. This number should be used when referring to the figure in the text. Figure references should be included within the text in numerical order according to their order of appearance. Figure may be referenced within the text as "Fig.-x". When the reference to a figure begins a sentence, the abbreviation "Fig," should be spelled out e.g., "Figure-x"

Tables

All tables should be numbered consecutively. Tables should have a caption consisting of the table number and brief title. This number should be used when referring to the table in text. Table references should be included within the text in numerical order according to their order of appearance. Table should be inserted as part of the text as close as possible to its first reference.

Acknowledgments

All individuals or institutions not mentioned elsewhere in the work who have made an important contribution should be acknowledged.

References

Within the text, references should be cited with name of the author and year in parenthesis. The reference list will be arranged alphabetically.

Example

Chamber (1959) has described a method and Wormleaton (2006) used this method. In case of two authors, name of both the authors will appear with year. For example Khan and Ghumman (2008) studied hydrodynamic modeling for water-saving strategies in irrigation canals. In case of three or more authors it will be cited as: Ghumman et al. investigated use of numerical modeling for management of canal irrigation water in case of continuous references, the references may be separated by comma", " See the list of sample references.

List of References

References to original source of the cited material as given above as sample reference should be listed together at the end of the paper, footnotes should not be used for this purpose. References should be arranged in alphabetic order. Each reference should include the last name of each author followed by his initials.

1. Reference to journal articles and paper in serial publication include :Last name of each author followed by their initial, Year of publication, Full title of the cited article, Full name of the publication in which it appears, Volume number (if any) in boldface, Issue number (if any) in parentheses, Inclusive page number of the cited article.
2. Reference to the text books and monographs should include: Last name of each author followed by their initial, Year of publication, Full title of the publication, Publisher, City of publication, Inclusive page number of the work being cited, Chapter number(if any).
3. Reference to original conference papers, papers in compiled conference proceedings or any other collection of woks by numerous authors should include: Last name of each author followed by their initial, Year of publication, Full title of the cited paper in quotes, individual paper number (if any) ,Full title of the publication , Initial followed by the name of the editor (if any),followed by the abbreviation, "eds" ,Publisher, City of publication, Volume number (if any),Inclusive Page number of the work being cited.
4. Reference to thesis and technical reports should include: Last name of each author followed by their initial, Year of publication, Full title in quotes, title capitalization, Report number(if any) Publisher or the institution name, City.

Sample References

- [1] Bievre B.D Alvarado, A.Timbe, L. Celleri and J. Feyen 2003.Night irrigation reduction for water saving in medium-sized system, Journal of irrigation and Drainage Engineering, ASCE Vol.129, NO.2.337-348.
- [2] Chamber R.1988. Managing canal irrigation: Practical Analysis from South Asia, Institution of Development Studies, Oxford & IBH Publishing Co. Ltd.
- [3] Strelkof T.1969.One-dimentional equations of open-channel flow. J. Hydraulics Div., ASCE, Vol.95 (HY3):861-876
- [4] Khan,M.Z. 2006. Investigation of the optimal operation strategies for irrigation systems. Ph.D.Dissertation. Department of Civil Engineering, University of Engineering and Technology Taxila.
- [5] Ghumman, A.R., M.Z. Khan, and M.J. Khan.2006.Use of numerical Modeling for Management of Canal Irrigation Water. Irrigation and Drainage.Wilay Intersciencez. : 445-458.
- [6] Khan M. Z. and Ghumman A. R.2008, Hydrodynamic Modeling For Water-Saving Strategies In Irrigation Canals.

